

# Geochemistry, Geophysics, Geosystems

## RESEARCH ARTICLE

10.1029/2018GC008120

### Key Points:

- Sill geometry and emplacement depth as well as intruded host-rock type are the main factors controlling methane mobilization and degassing
- Dehydration-related porosity increase and pore pressure-induced hydrofracturing are important mechanisms for a quick transport of methane from sill to the surface
- The Karoo Basin may have degassed  $\sim 22.3 \cdot 10^3$  Gt of thermogenic methane in the half million years of magmatic activity

### Supporting Information:

- Supporting Information S1
- Table S3

### Correspondence to:

C. Y. Galerne,  
cgalerne@geomar.de

### Citation:

Galerne, C. Y., & Hasenclever, J. (2019). Distinct degassing pulses during magma invasion in the stratified Karoo Basin—New insights from hydrothermal fluid flow modeling. *Geochemistry, Geophysics, Geosystems*, 20, 2955–2984. <https://doi.org/10.1029/2018GC008120>



Received 10 DEC 2018

Accepted 10 APR 2019

Accepted article online 3 JUN 2019

Published online 25 JUN 2019

## Distinct Degassing Pulses During Magma Invasion in the Stratified Karoo Basin—New Insights From Hydrothermal Fluid Flow Modeling

C. Y. Galerne<sup>1</sup>  and J. Hasenclever<sup>2</sup> 

<sup>1</sup>GEOMAR Helmholtz Centre for Ocean Research Kiel, Kiel, Germany, <sup>2</sup>Institute of Geophysics, Hamburg University, Hamburg, Germany

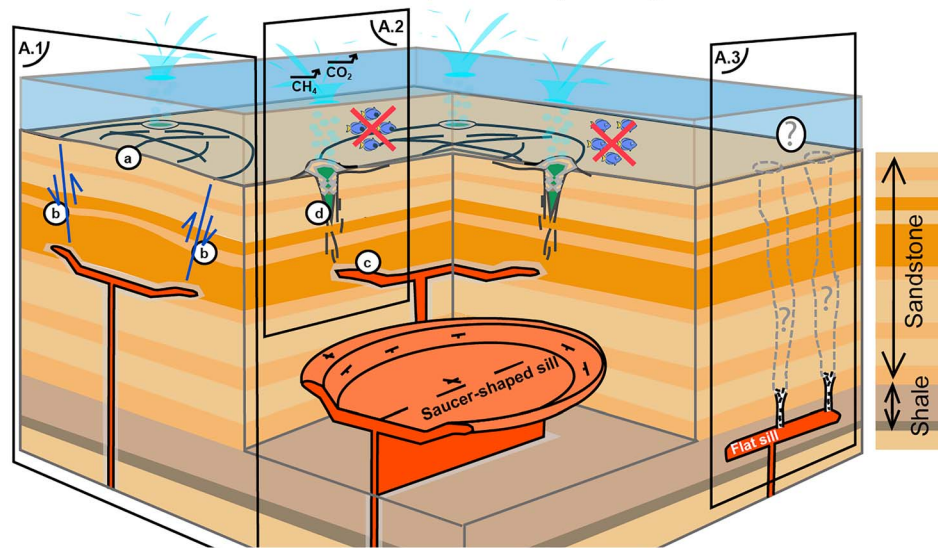
**Abstract** Magma emplacement in organic-rich sedimentary basins is a main driver of past environmental crises. Using a 2-D numerical model, we investigate the process of thermal cracking in contact aureoles of cooling sills and subsequent transport and emission of thermogenic methane by hydrothermal fluids. Our model includes a Mohr-Coulomb failure criterion to initiate hydrofracturing and a dynamic porosity/permeability. We investigate the Karoo Basin, taking into account host-rock material properties from borehole data, realistic total organic carbon content, and different sill geometries. Consistent with geological observations, we find that thermal plumes quickly rise at the edges of saucer-shaped sills, guided along vertically fractured high-permeability pathways. Contrastingly, less focused and slower plumes rise from the edges and the central part of flat-lying sills. Using a novel upscaling method based on sill-to-sediment ratio, we find that degassing of the Karoo Basin occurred in two distinct phases during magma invasion. Rapid degassing triggered by sills emplaced within the top 1.5 km emitted  $\sim 1.6 \cdot 10^3$  Gt of thermogenic methane, while thermal plumes originating from deeper sills, carrying a 13-times-greater mass of methane, may not reach the surface. We suggest that these large quantities of methane could be remobilized by the heat provided by neighboring sills. We conclude that the Karoo large igneous province may have emitted as much as  $\sim 22.3 \cdot 10^3$  Gt of thermogenic methane in the half million years of magmatic activity, with emissions up to 3 Gt/year. This quantity of methane and the emission rates can explain the negative  $\delta^{13}\text{C}$  excursion of the Toarcian environmental crisis.

### 1. Introduction

Degassing of an organic-rich sedimentary basin intruded by a large igneous province (LIP) plumbing system is a potential source of atmospheric forcing volatiles, which is nearly 10 times greater than any other volcanic related sources. Jones et al. (2016) estimate a release of up to 70 Mt carbon (C) per cubic kilometer of magma emplaced based on various studies of the Karoo LIP (Aarnes et al., 2010, 2011; Svensen et al., 2007). This process is now broadly accepted as one of the main driving mechanisms for rapid climate change and mass extinction (e.g., Aarnes et al., 2010; Ganino & Arndt, 2009) such as the End-Permian (Siberian Traps, Heydari et al., 2008; Retallack & Jahren, 2008; Svensen et al., 2009), the End-Triassic (Central Atlantic Magmatic Province, e.g., Blackburn et al., 2013; Jones et al., 2016), the Toarcian (Karoo-Ferrar LIP, Svensen et al., 2007, 2012; Burgess et al., 2015), the Palaeocene-Eocene Thermal Maximum (Northeast Atlantic Igneous Province, e.g., Svensen et al., 2004), and the mid-Miocene climatic optimum associated with the Columbia River Basalt (McKay et al., 2014). Traces of violent release of thermogenic gases at the basin top are found in the form of pipe-like structures that root to the contact aureole of the sill intrusions at depth (Figure 1). These sill complexes have been extensively documented through seismic imaging (e.g., Berndt et al., 2016; Cartwright & Hansen, 2006; Hansen & Cartwright, 2006; Hansen et al., 2004; Planke & Symonds, 2000; Svensen et al., 2004; Thomson, 2005, 2007; Thomson & Hutton, 2004). On land, sill complexes and related hydrothermal vent complexes (HVCs) outcrop in eroded basins such as the Karoo Basin in South Africa (Svensen et al., 2006, 2007) and the Tunguska Basin in Russia (Svensen et al., 2009). However, despite their evident control on the basin degassing rates, HVCs and the processes that lead to the formation of high-permeability pathways remain unaccounted for in quantitative assessments of thermogenic gas emission to the ocean floor.

HVCs observed in 2-D and 3-D seismic studies can be traced down to the upper rim of saucer-shaped sills (e.g., Berndt et al., 2016; Planke et al., 2005), and it is commonly accepted that this type of sill geometry acts as a major

**A. Established relation between sill complexes and piercing structures**



**B. Magma emplacement in strong and weak host-rock material**

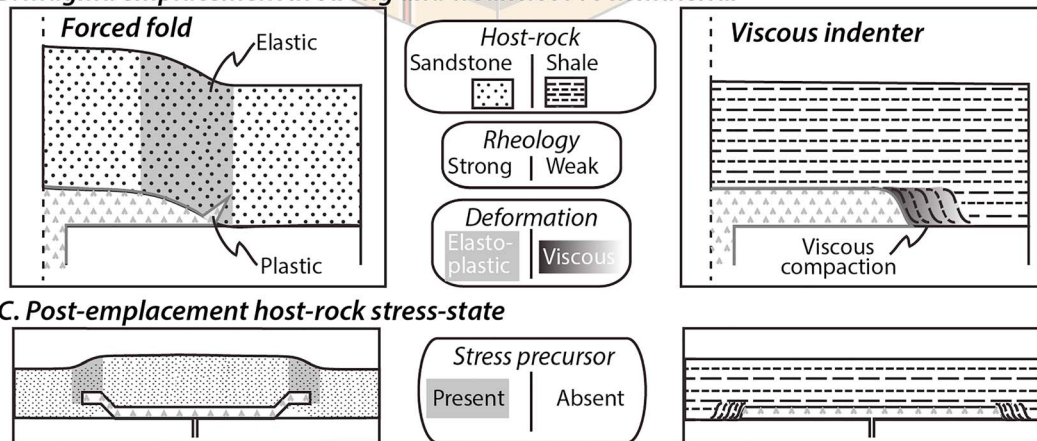


**Figure 1.** (A) Processes associated with sill emplacement in sedimentary basins. (A.1) Sill emplacement in sandstone dominated lithologies and forced fold mechanism: (a) Smooth dome structure related to the deformation by saucer-shaped sill emplacement at depth (e.g., Galland, 2012). (b) Shear bands develop at the edge of the uplifted overburden. (A.2) Hydrothermal vent complexes: (c) Contact metamorphism develops an aureole around sills and mobilizes large volumes of greenhouse gases (e.g., Svensen et al., 2004). (d) Pipe outlet of hydrothermal vent complexes pierces through the ocean floor, liberating thermogenic gases into the ocean-atmosphere system (e.g., Jamtveit et al., 2004). (A.3) Sill emplacement in shale-dominated lithologies and potentially associated breccia pipes with more random distribution. (B, C) Examination of the impact of the rheological response of different sedimentary host-rocks during magma emplacement (B) and implications for the overburden post-emplacement stress state (C). Left column considers a strong sandstone host-rock material; right column considers a weak shale host-rock material.

controlling parameter in the formation and distribution of HVCs (Figure 1A). Other fluid pathways identified as breccia pipes have been mapped in the deep parts of organic-rich basins like the Karoo in South Africa. However, their distribution in a map view appears random and thus contrasts with the prominent circular pattern formed by HVCs that highlight the contour of saucer-shaped sills (e.g., Berndt et al., 2016).

To understand the relation between HVCs and breccia pipes to sill complexes, we rely on the following observations from the Karoo Basin. HVCs are identified near the basin top in sandstone-dominated formations hosting saucer-shaped sills, while breccia pipes are identified in the deep part of the basin in shale dominated formations hosting flat-lying sills. This relation between sill geometry and host-rock material can be explained in a simple end-member rheological model. Saucer-shaped sill geometries form when an invading magma acts as an inflating viscous phase at the base of a coherently elastic overburden such as a sandstone lithology (Figures 1A and 1B; e.g., Galland & Scheibert, 2013). The uplifted material results in surface doming of the basin—a deformation process known as forced folding (Figures 1A.1; Hansen & Cartwright, 2006, 2007;

Galland et al., 2009; Schmiedel et al., 2017; Galland et al., 2018). The final saucer-shape is acquired when the yield strength of the bending plate is overcome at the front of the propagating sill so that inclined magmatic sheets transgress upward and outward through the overburden (Figures 1A.1 and 1B; Pollard & Johnson, 1973; Malthe-Sørenssen et al., 2004; Galland et al., 2009; Haug et al., 2018).

In contrast, space accommodation for a magma invading into less cohesive shale occurs mostly laterally. Considering a case where a shale formation is encased above and below by stronger formations, a flat sill will form through lateral compaction of the shale (Figure 1B). This latter accommodation process, called “viscous indenter” (Figure 1B; Merle & Donnadieu, 2000; Mathieu et al., 2008; Abdelmalak et al., 2012; Spacapan et al., 2016), concentrates the deformation locally at the tip of the propagating sill, while in the former saucer-shaped sill case a larger deformation affects the overburden up to the basin top (Figure 1C).

The current research challenge lies with establishing a causal link between LIP emplacement and degassing of an organic-rich basin. The goal is to precisely quantify the amount and rates at which thermogenic gases are mobilized and released by venting into the ocean and/or atmosphere. To that end, conductive heat flow models have been developed to simulate the devolatilization process considering the exothermic process of magma crystallization and the endothermic processes of kerogen cracking and dehydration reactions (Aarnes et al., 2010). A calibrated kerogen cracking model considering the breaking of different kerogen bounds (Sweeney & Burnham, 1990) allows to calculate the amount of thermogenic gas that is converted from the total organic carbon (TOC) present in the host-rock. This kerogen cracking model has been used to estimate the degassing caused by contact metamorphism within the contact aureole around cooling sills (Iyer et al., 2018; Iyer et al., 2017; Iyer et al., 2013; Aarnes et al., 2015; Aarnes et al., 2011; Aarnes et al., 2010; Kjeldstad et al., 2003). To provide a potential basin-scale degassing estimate, the surface area of sill intrusions in the sedimentary basin of interest, for example,  $\sim 85,000$  km<sup>2</sup> in the Vøring and Møre Basins (offshore Norway, Svensen et al., 2004) and  $\sim 370,000$  km<sup>2</sup> in the Karoo Basin (South Africa, Svensen et al., 2017), is used to upscale the quantitative results obtained from a single cooling sill model (e.g., Aarnes et al., 2010; Iyer et al., 2013). These types of numerical studies establish that the LIP event that intruded the Karoo Basin potentially mobilized  $\sim 2,700$ – $16,200$  Gt CH<sub>4</sub> (Aarnes et al., 2010), while the magmatic event of the North Atlantic Province potentially mobilized  $\sim 600$ – $3,500$  Gt CH<sub>4</sub> from the Vøring and Møre Basins (Aarnes et al., 2010). Subsequent studies that additionally accounted for heat transport by hydrothermal fluid flow (Iyer et al., 2013, 2017) have estimated that the total amount of thermogenic gas mobilized by organic cracking and emitted at the top of these intruded sedimentary basins is sufficient to trigger an environmental crisis.

The goal of our study is to address two important aspects that have been neglected by the above-mentioned studies. First, sediment dehydration and hydrothermal fluid flow cause high pore pressures that can locally lead to mechanical failure of the host-rock, especially if the rock is prestressed by the magma emplacement. This process may be key for the formation of high-permeability channels that affect basin-scale degassing rates. Second, thick sedimentary basins are always stratified and often show significant depth variations in rheological, hydraulic, and thermal material properties as well as, most importantly, in TOC content. Such variations cannot be accounted for when upscaling single numerical calculations to basin scale.

In our study, we have introduced a failure criterion using a simple Mohr-Coulomb rheology that—coupled to pore pressure in the hydrothermal system—promotes hydrofracturing and the formation of high-permeability pathways. The pre-existing host-rock stress state (Figure 1C), which is directly related to the host-rock type and the magma emplacement process, plays an important role in this hydrofracturing process. Furthermore, we explicitly account for the porosity increase associated with host-rock dehydration, which directly affects the rock permeability and hence the fluid flow patterns. These improvements have been implemented in a state-of-the-art 2-D numerical model for hydrothermal fluid flow through porous rocks (e.g., Hasenclever et al., 2014). We consider borehole data (Svensen et al., 2018) to constrain the sill proportion with respect to their host sedimentary rock at the basin scale. Important petrophysical host-rock properties are derived from stratigraphic studies of the Karoo (e.g., Johnson et al., 2006), while hydraulic properties are derived from measured porosity (Baiyegunhi et al., 2014). Finally, we constructed a realistic initial TOC profile based on various sources (EIA, 2015; Branch et al., 2007; Faure & Cole, 1999). Our model is applied to one of the best documented organic-rich basins intruded by a LIP plumbing system, the Karoo

Basin in South Africa (Figure 2). In a set of model calculations, we investigate sills at various depths within different lithologies. Our new quantitative results of thermogenic degassing are discussed in the perspective of the Toarcian environmental crisis and more globally as a geological forcing mechanism for paleo-environmental crises associated with LIP volcanism.

## 2. A Window Into a LIP Plumbing System: The Karoo Basin, South Africa

The Karoo Basin is part of the Jurassic basin system that developed at the southern margin of Gondwana (e.g., Catuneanu et al., 1998; Johnson et al., 2006). It covers most of present-day South Africa and is bounded in the South by the Cape Fold Belt (Johnson et al., 2006). The basement is made of the Archean Kaapval craton, shielded in the South by a Proterozoic basement (Tankard et al., 2009). The 5- to 6-km clastic sedimentary strata are capped by 1.5 km of basaltic lavas that are the surface expression of the Karoo LIP magmatism (Figure 2A). The Karoo LIP includes a vast plumbing system of magma intrusions emplaced throughout the Karoo Basin stratigraphy (Chevallier & Woodford, 1999; Galerne et al., 2008). The magmatic event of the Karoo has marked the end of the basin subsidence at 183 Ma (Catuneanu et al., 1998). The present-day exhumed Karoo Basin offers a window on the entire basin stratigraphy and exposes the Karoo LIP plumbing system and associated HVCs (Figures 1A and 2A).

The most organic-rich formations of the Karoo Basin are located in the Ecca Group (Gp.) and include the black shale formations of the Prince Albert, Whitehill, and Tierberg Formations. These formations are reported to have considerable variations in TOC from 1.10 to 15 wt.%, locally reaching up to 18 wt.% in the Whitehill Formation (Branch et al., 2007; Faure & Cole, 1999). Due to the overall high TOC contents of the Ecca Gp., the lower part of the Karoo stratigraphy has been identified as the most significant source of methane-rich fluids potentially mobilized by contact metamorphism (e.g., Aarnes et al., 2011).

With the exception of the Stormberg Gp., sills and saucer-shaped sills clearly dominate the overall intrusive system of the Karoo in comparison to the relatively rare dykes (e.g., Chevallier & Woodford, 1999). Sills and saucer-shaped sills are in general >10 km in diameter in the deepest stratigraphy, while smaller sills of  $\leq 10$  km in diameter intruded the upper part of the Karoo stratigraphy (Chevallier & Woodford, 1999; Du Toit, 1920). Sill thicknesses vary between 50 and 150 m (Galerne et al., 2008; Chevallier & Woodford, 1999; Galerne et al., 2010).

Hundreds of cylindrical piercing structures identified as breccia pipes and HVCs have been mapped in the Karoo Basin (e.g., Svensen et al., 2007). The breccia pipes are exclusively observed in the lower Ecca Gp. (Svensen et al., 2007; Woodford et al., 2001) and are commonly up to 50–80 m in diameter (Woodford et al., 2001). In contrast, HVCs are represented only in the upper Beaufort Gp. and Stormberg Gp. They are characterized by structures of up to 300 m in diameter of inward dipping concentric structures (Svensen et al., 2006). HVCs are generally found at the base of the extrusive basalts but rarely cut through, although some phreatomagmatic complexes have been reported to postdate the earliest flood basalts (Stockley, 1947). Consequently, these phreatic types of eruptions are interpreted as dominantly predating the flood basalt eruptions (Svensen et al., 2006) within a significant ambient water column. Similar phreatomagmatic eruptions in the twin magmatic province Ferrar in Antarctica consistently predate the main effusive phase suggesting a similar sequence of events in both provinces (Hanson & Elliot, 1996; White & McClintock, 2001).

## 3. Model Description

### 3.1. Hydrothermal Model

We use a 2-D finite element model (Hasenclever et al., 2014) to simulate hydrothermal fluid flow triggered by a magmatic sill intrusion. The model solves for the thermal evolution of the sill and surrounding host-rock as well as the flow of water through porous rocks. For this study, we have improved the model by Hasenclever et al. (2014) by considering (1) the conversion of organic matter, (2) the devolatilization of sediments and associated increase in porosity, (3) the transport of methane dissolved in the pore fluid, and (4) hydrofracturing. In the following, we will describe the governing equations. Indices  $f$  and  $r$  refer to fluid and rock properties, respectively. All fluid properties are functions of both pressure and temperature and

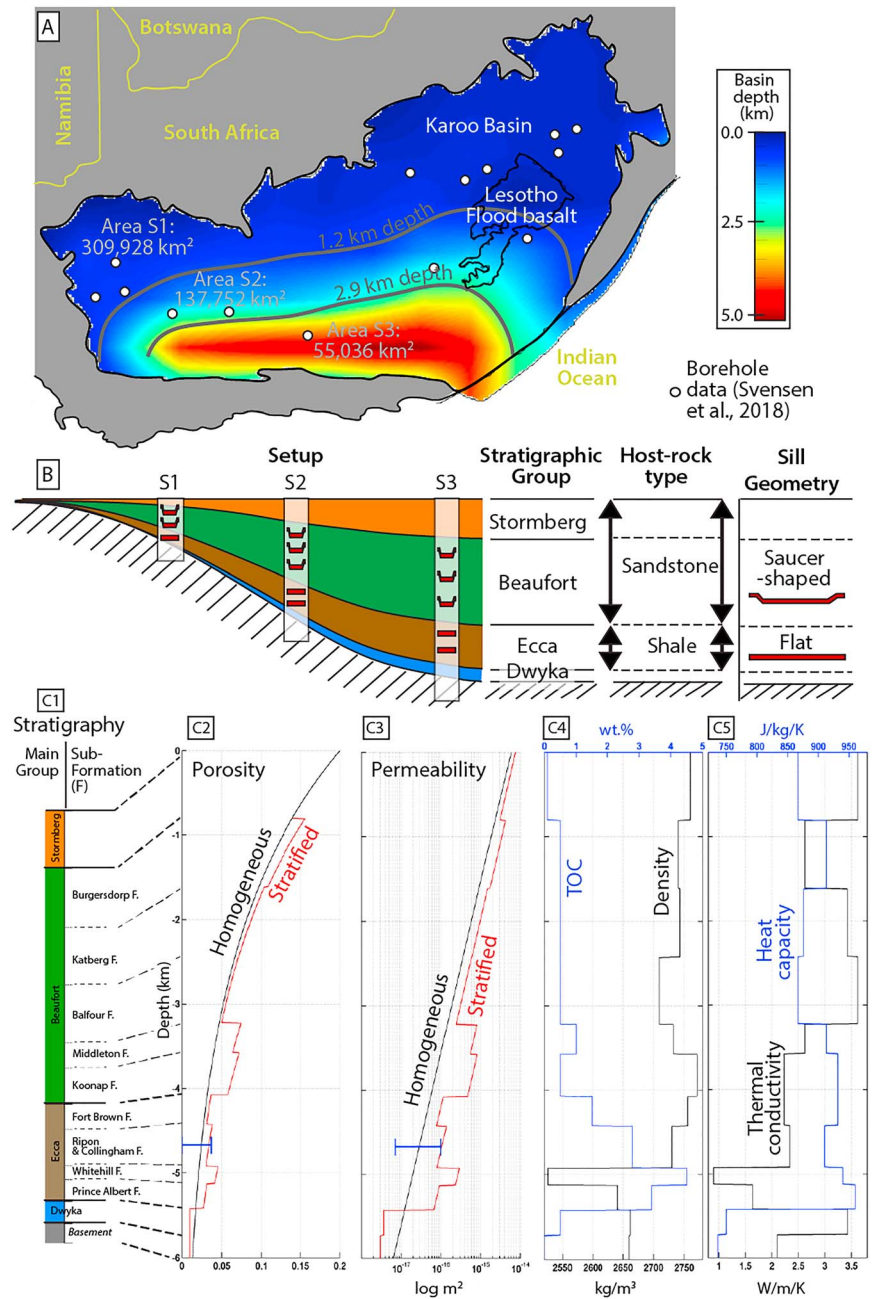


**Figure 2.** (A) Depth map of the Karoo Basin sediment thickness extracted from the Laske et al., (2013) database. The gray isocontours at 1.2- and 2.9-km depths separate three areas: the shallowest sedimentary section of the basin represented by Area S1 (corresponding profile S1 in B), medium depth section represented by Area S2 (corresponding profile S2 in B), and deepest section of the basin represented by Area S3 (corresponding profile S3 in B). (B) Corresponding 2-D section of the Karoo Basin highlights the three representative stratigraphic sections considered. For simplicity, the main stratigraphic groups are assumed to linearly decrease from the deepest section to the shallowest. The sill emplacement levels considered for each section are sketched, together with the sill geometry controlled by the host-rock type: Sandstone imposes saucer-shaped geometry, while shale imposes flat-lying sill geometry. (C) Reference synthetic stratigraphic log of the Karoo Basin representing a typical Eastern Cape sedimentary section. (C1) The stratigraphic units used to define the host-rock material properties in each formation (Catuneanu et al., 1998; Johnson et al., 2006). (C2) Initial porosity calculated with equation (10) using measurements by Baiyegunhi et al. (2014). The porosity range from the Ecca formation is indicated in blue (Campbell, Lenhardt, et al., 2016). (C3) Initial permeability calculated using equation (11) with reported corresponding permeability range after Campbell, Lenhardt, et al. (2016). (C4) Initial weight percent total organic carbon profile; see text for details. (C5) Density values from Baiyegunhi et al. (2014); thermal conductivity and heat capacity are taken from Čermák and Rybach (1982).

are evaluated from precalculated lookup tables based on the IAPWS-84 formulation. A complete list of symbols with corresponding values and units is given in Table 1.

We consider porous flow of pure water through a rigid medium. Throughout the calculations, pore pressures are above the critical point of pure water so that the fluid remains in a single-phase state. Our single-phase hydrothermal model requires this assumption, because in the system  $\text{H}_2\text{O}-\text{NaCl}-\text{CO}_2-\text{CH}_4$  phase transitions would be possible even at higher pressures. We will discuss potential consequences of this simplification later. Fluid flow is described by Darcy's law

$$\vec{v}_f = -\frac{K}{\mu_f} (\nabla P - \rho_f \vec{g}) \quad (1)$$

where  $\vec{v}_f$  is the Darcy velocity,  $K$  is the rock's permeability,  $\mu_f$  is the fluid's dynamic viscosity,  $\rho_f$  is the fluid's density,  $P$  is pore pressure, and  $\vec{g}$  is the gravitational acceleration vector. The equation for pore pressure is derived from mass conservation under the assumption that the compressibility of the rock is several orders of magnitude lower than that of the fluid and hence negligible. However, we do consider temporal changes of porosity  $\phi$  due to dehydration reactions of the host-rock. Mass conservation is hence expressed as

$$\frac{\partial(\phi\rho_f)}{\partial t} = \phi \frac{\partial\rho_f}{\partial t} + \rho_f \frac{\partial\phi}{\partial t} = -\nabla \cdot (\rho_f \vec{v}_f) + R_{\text{H}_2\text{O}} + R_{\text{CH}_4} \quad (2)$$

with  $R_{\text{H}_2\text{O}}$  being a source term from mass of fluid released into the pore space by dehydration of the host-rock and  $R_{\text{CH}_4}$  being the mass of methane released into pore space during organic cracking (also discussed below).

Substituting equation (1) into equation (2) and rearranging yields

$$\phi \frac{\partial\rho_f}{\partial t} = \nabla \cdot \left[ \rho_f \frac{K}{\mu_f} (\nabla P - \rho_f \vec{g}) \right] - \rho_f \frac{\partial\phi}{\partial t} + R_{\text{H}_2\text{O}} + R_{\text{CH}_4} \quad (3)$$

We use a fully compressible formulation so that the fluid's density is a function of both temperature  $T$  and pressure, that is,  $\frac{\partial\rho_f}{\partial t} = \rho_f (\beta_f \frac{\partial P}{\partial t} - \alpha_f \frac{\partial T}{\partial t})$ , where  $\alpha_f$  and  $\beta_f$  are the fluid's thermal expansivity and compressibility, respectively, so that we obtain

$$\phi\rho_f\beta_f \frac{\partial P}{\partial t} = \nabla \cdot \left[ \rho_f \frac{K}{\mu_f} (\nabla P - \rho_f \vec{g}) \right] + \phi\rho_f\alpha_f \frac{\partial T}{\partial t} - \rho_f \frac{\partial\phi}{\partial t} + R_{\text{H}_2\text{O}} + R_{\text{CH}_4}. \quad (4)$$

We solve equation (4) with an implicit finite element method to obtain the pressure field. With the pressure solution, we obtain the Darcy velocity field using equation (1).

To obtain the temperature evolution, we solve for energy conservation considering temporal changes in porosity

$$\frac{\partial}{\partial t} [(\phi\rho_f c_{pf} + (1-\phi)\rho_r c_{pr})T] = \nabla \cdot (k_r \nabla T) - \vec{v}_f \cdot \nabla T + \frac{\mu_f}{K} \vec{v}_f^2 - \left( \frac{\partial \ln \rho_f}{\partial \ln T} \right)_p \frac{DP}{Dt} + Q \quad (5)$$

with  $c_p$  being specific heat capacity and  $k_r$  thermal conductivity of the rock.  $Q$  summarizes all heat sources and sinks (discussed below). Fluid and rock are assumed to be in local thermal equilibrium (that is,  $T = T_r = T_f$ ) so that the porosity-weighted mixture appears on the left-hand side of equation (5). Changes in temperature depend on heat conduction (first term on the right-hand side), heat advection by fluid flow (second term), heat generation by internal fluid friction (third term), the pressure-volume work of the fluid (fourth term), and heat sources and sinks (fifth term). Details can be found in Hasenclever et al. (2014) and its supplement. Rearranging the terms in equation (5) yields

$$(\phi\rho_f c_{pf} + (1-\phi)\rho_r c_{pr}) \frac{\partial T}{\partial t} = \nabla \cdot (k_r \nabla T) - \vec{v}_f \cdot \nabla T + \frac{\mu_f}{K} \vec{v}_f^2 - \left( \frac{\partial \ln \rho_f}{\partial \ln T} \right)_p \frac{DP}{Dt} + Q - (\rho_f c_{pf} - \rho_r c_{pr}) T \frac{\partial\phi}{\partial t} \quad (6)$$

which we solve using operator splitting. The advection term is treated with a semi-Lagrange advection scheme, while all other terms are handled by an implicit finite element method. The term  $Q$  in

**Table 1**  
*List of Parameters and Variables in the 2-D Model*

Symbol	Description	Value	Unit
<b>Primary variables</b>			
$x$	Horizontal coordinate		m
$z$	Vertical coordinate		m
$t$	Time	—	s
$\Delta t$	Time step in numerical calculation	—	s
$\vec{g}$	Gravitational acceleration	9.81	$\text{m/s}^2$
$P$	Pore pressure	—	Pa
$T$	Temperature	—	$^{\circ}\text{C}$
$\vec{v}_f$	Darcy velocity	equation (1)	m/s
$\vec{u}_f$	Pore velocity	$= \vec{v}_f / \phi$	m/s
$Q$	Heat sources/sinks in energy equation	equation (7)	$\text{J}\cdot\text{m}^{-3}\cdot\text{s}^{-1}$
<b>Temperature- and pressure-dependent fluid properties</b>			
$\mu_f$	Dynamic viscosity	EOS	$\text{Pa}\cdot\text{s}$
$\rho_f$	Density	EOS	$\text{kg/m}^3$
$c_{pf}$	Specific heat capacity	EOS	$\text{J}\cdot\text{kg}^{-1}\cdot\text{K}^{-1}$
$\alpha_f$	Thermal expansion coefficient	EOS	$\text{K}^{-1}$
$\beta_f$	Compressibility	EOS	$\text{Pa}^{-1}$
<b>Host-rock material properties (see stratigraphic log data)</b>			
$\rho_r$	Density	Figure 2C	$\text{Pa s}$
$c_{pr}$	Specific heat capacity	Figure 2C	$\text{J}\cdot\text{kg}^{-1}\cdot\text{K}^{-1}$
$k_r$	Thermal conductivity	Figure 2C	$\text{W}\cdot\text{m}^{-1}\cdot\text{K}^{-1}$
$\Phi$	Porosity	Figure 2C	1
$\Phi_0$	Porosity at reference depth $z = 0$	Figure 2C	1
$b$	Exponent in equation (10)	$0.45\cdot 10^{-3}$	$\text{m}^{-1}$
$K$	Permeability	equation (11), Figure 2C	$\text{m}^2$
$K_0$	Reference permeability at depth $z = 0$	$3\cdot 10^{-13}$	$\text{m}^2$
$n$	Exponent in Kozeny-Carman equation, equation (11)	1.5	1
$\text{TOC}$	Initial total organic carbon	Figure 2C	$\text{kg (TOC)/kg}$
$T_{\text{brittle}}$	Lower limit of brittle-ductile-transition	500	$^{\circ}\text{C}$
$T_{\text{ductile}}$	Upper limit of brittle-ductile-transition	750	$^{\circ}\text{C}$
$C$	Cohesion (sandstone/shale)	27.2/38.4	MPa
$\theta$	Angle of internal friction (sandstone/shale)	27.8/14.4	$^{\circ}$
$\sigma_1, \sigma_3$	Largest/smallest principle stress	—	Pa
$\sigma_{\text{diff}}$	Differential stress	$= \sigma_1 - \sigma_3$	Pa
$\sigma_m$	Mean stress	$= (\sigma_1 + \sigma_3) / 2$	Pa
$\tau$	Shear strength	equation (20)	Pa
$A$	Ratio smallest/largest principle stress	$= \sigma_3 / \sigma_1$	1
$F_{\text{shear}}$	Pressure required to enable shear failure mode	equation (21)	Pa
$F_{\text{tensile}}$	Pressure required to enable tensile failure mode	equation (22)	Pa
$P_{\text{fail}}$	Pore pressure required to initiate hydrofracturing	equation (23)	Pa
$\lambda$	Ratio between pore pressure and failure pressure	equation (24)	1
$a$	Exponent controlling permeability increase, equation (25)	2	1
$L_{\text{H}_2\text{O}}$	Enthalpy of mineral dehydration	2,800	$\text{kJ/kg(H}_2\text{O)}$
$R_{\text{H}_2\text{O}}$	Rate of fluid mass released into pore space	equation (8)	$\text{kg(H}_2\text{O)}\cdot\text{m}^{-3}\cdot\text{s}^{-1}$
$L_{\text{OM}}$	Enthalpy of organic cracking	375	$\text{kJ/kg(TOC)}$
$R_{\text{OM}}$	Rate of organic cracking	equation (15)	$\text{kg (TOC)}\cdot\text{m}^{-3}\cdot\text{s}^{-1}$
$R_{\text{CH}_4}$	Rate of methane release into pore space	equation (16)	$\text{kg (CH}_4\text{)}\cdot\text{m}^{-3}\cdot\text{s}^{-1}$
$w_{\text{H}_2\text{O}}$	Water content of host-rock	—	wt.%
$F_{\text{OM}}$	Total converted fraction of organic material	equation (12)	1
$\%R_0$	Vitrinite reflectance	equation (13)	1
$w_{\text{OM}}$	Remaining convertible organic material	equation (14)	$\text{kg (TOC)/kg}$
$m_{\text{C/CH}_4}$	Conversion factor from carbon to methane	1.34	$\text{kg/kg}$
$M_{\text{CH}_4}$	Mass of methane	equation (17)	$\text{kg/m}$
<b>Magma/sill properties</b>			
$T_m$	Initial temperature of sill	1150	$^{\circ}\text{C}$
$T_L$	Liquidus temperature	1150	$^{\circ}\text{C}$
$T_S$	Solidus temperature	950	$^{\circ}\text{C}$
$h$	Thickness of sill	100	m
$\rho_m$	Density of magma/sill	2,830	$\text{kg/m}^3$
$k_m$	Thermal conductivity of magma/sill	2.8	$\text{W}\cdot\text{m}^{-1}\cdot\text{K}^{-1}$

**Table 1**  
(continued)

Symbol	Description	Value	Unit
$c_{pm}$	Specific heat capacity of magma/sill	900	$\text{J}\cdot\text{kg}^{-1}\cdot\text{K}^{-1}$
$\Phi_C$	Crystal fraction in magma	equation (18)	1
$L_C$	Enthalpy of fusion (latent heat of crystallization)	320	$\text{kJ}/\text{kg}$
$R_C$	Rate of crystallization	equation (19)	$\text{kg}\cdot\text{m}^{-3}\cdot\text{s}^{-1}$

equation (6) includes the energy released by magma crystallization (index C) and the energy consumed during cracking of organic matter (index OM) and dehydration of the host-rock (index H<sub>2</sub>O):

$$Q = L_C R_C - L_{OM} R_{OM} - L_{H_2O} R_{H_2O} \quad (7)$$

Here  $L$  denotes the total enthalpy associated with the completion of the process (see Table 1) and  $R$  denotes the rate, in units of kilograms per cubic meter per second, at which each process or reaction takes place. Note that crystallization of magma is exothermic and releases latent heat, while conversion of organic matter and devolatilization are endothermic processes and consume energy.

Equations (6) and (7) pose a nonlinear problem because (7) appears on the right-hand side of (6), while the rates in (7) depend on the temperature evolution obtained with equation (6). We solve this nonlinearity by iteratively solving equation (6) and recalculating equation (7) until a consistent solution for temperature and the rates of magma crystallization, organic matter conversion, and host-rock dehydration has been derived. Convergence of this iterative thermo-reactive scheme is usually achieved within three to five iterations.

### 3.2. Porosity-Permeability Relation and Host-Rock Dehydration

The dehydration of the host-rock is calculated as a temperature-dependent process. Using the thermodynamic code *Perple\_X* (Connolly, 2009), we calculate the stable mineral assemblage for an average pelite composition (a composition identical to that used by Aarnes et al., 2010) as a function of temperature (0 to 1200 °C) and pressure (0 to 300 MPa). From this phase diagram (see Figure 4b in Aarnes et al., 2010), we determine the maximum weight fraction of water,  $w_{H_2O}$ , that can be stored in the mineral assemblage. The pressure range in our model calculations is 25 to ~100 MPa, and here the maximum water content is mainly a function of temperature. For simplicity, we neglect the pressure dependence and use a temperature-dependent profile at 85 MPa (supporting information S1). We assume that all host-rock types contain initially 5-wt.% water and follow the same temperature-dependent dehydration path. The rate of dehydration,  $R_{H_2O}$ , is calculated from the change in maximum water content storable in the mineral assemblage of the rock:

$$R_{H_2O} = -(1-\phi)\rho_r \frac{\partial w_{H_2O}}{\partial t} \quad (8)$$

The temporal change in porosity is directly related to the dehydration rate of the host-rock:

$$\frac{\partial \phi}{\partial t} = -(1-\phi) \frac{\partial w_{H_2O}}{\partial t} \quad (9)$$

Note that the dehydration rate  $R_{H_2O}$  is defined to be positive for dehydration and cannot be negative since we do not consider rehydration of the host-rock.

To calculate the initial porosity profile as function of depth we use Athy's formulation (Athy, 1930)

$$\phi(z) = \phi_0 \cdot e^{(-b \cdot z)} \quad (10)$$

where  $\phi_0$  is the porosity of a given host-rock material at reference depth ( $z = 0$  km),  $z$  is the actual depth, and  $b$  is a constant characterizing the compressibility of the host-rock material. The porosity calculated with equation (10) represents the initial state. Dehydration of the sediments leads to an increase in pore space



according to equation (9). This process is assumed to be irreversible, and the host-rock is not allowed to rehydrate again. Permeability is defined as a function of porosity following the simplified Kozeny-Carman equation (Costa, 2006),

$$K(z) = K_0 \left[ \frac{\phi(z)^{n+1}}{(1-\phi(z))^n} \right] \quad (11)$$

where  $K_0$  is the reference permeability at the surface ( $z = 0$  km) and  $n = 1.5$  is a constant. Hence, permeability also increases irreversibly during dehydration of the host-rock.

### 3.3. Conversion of Organic Matter and Methane Generation

The rate of kerogen conversion into hydrocarbons is calculated using the calibrated model *Easy%Ro* by Sweeney and Burnham (1990). *Easy%Ro* calculates the total converted fraction as the sum of 20 reactions involved in the breaking down of the different kerogen bonds. See the model description by Sweeney and Burnham (1990) for details. For a given change in temperature from  $T(t)$  at time  $t$  to  $T(t+\Delta t)$  over a time interval  $\Delta t$ , the model calculates the total converted fraction of organic material:

$$F_{OM} = f(T(t), T(t + \Delta t), \Delta t) \quad (12)$$

Note that *Easy%Ro* assumes that only 85 % of the TOC is convertible so that at least 15% of organic material remains. The maturation of vitrinite is a kinetic process that relates to hydrocarbon generation. Although it depends on the chemistry of the kerogen involved, its value generally increases with the organic maturity of the source rock (Dow, 1977), which is mainly a temperature-controlled process. Hence, vitrinite reflectance (%Ro) is a good proxy to temperature and reflects the maximum temperature experienced by a rock. Following the parametrization of the *Easy%Ro* model (Iyer et al., 2013; Beardsmore & Cull, 2001; Aarnes et al., 2010; Sweeney & Burnham, 1990), we define

$$\%Ro = e^{(-1.6+3.7 \cdot F_{OM})} \quad (13)$$

The rate of thermogenic degassing is calculated by monitoring the evolution of the fraction of convertible organic material  $w_{OM}$  in the host-rock. Initially,  $w_{OM} = TOC$  is a host-rock-dependent value derived from the stratigraphic log data (see TOC profile in Figure 2C). Using the total converted fraction  $F_{OM}$  calculated with *Easy%Ro*, we calculate the remaining fraction of convertible organic material in the host-rock by

$$w_{OM} = (1-F_{OM}) \cdot TOC \quad (14)$$

The rate of kerogen conversion into hydrocarbons is given by the change in fraction of convertible organic material over time, that is,

$$R_{OM} = -\rho_r \frac{\partial w_{OM}}{\partial t} \quad (15)$$

In analogy to the dehydration rate, we define this rate to be positive for conversion so that  $R_{OM} \geq 0$ . The high temperatures in the contact aureole favor the transformation of organic matter into gaseous products rather than into liquid petroleum (e.g., Aarnes et al., 2010, and references therein). We thus assume that all hydrocarbon is converted into methane ( $CH_4$ ). The rate at which  $CH_4$  is released by the host-rock is calculated as

$$R_{CH_4} = m_{C/CH_4} R_{OM} \quad (16)$$

where  $m_{C/CH_4} = 1.34$  is the conversion factor from carbon to  $CH_4$ . We further assume that all released methane is dissolved in the pore fluid without affecting the fluid's physical and thermodynamic properties. This allows us to use the pressure- and temperature-dependent properties of pure water independent of the methane concentration. Iyer et al. (2013) showed that varying the density of methane-bearing fluids does not significantly affect the methane release rates at the surface, at least in single-phase flow models such as ours. Methane released by the host-rock is accumulated in and advected with the hydrothermal fluid according to

$$\frac{\partial}{\partial t} M_{\text{CH}_4} = -\nabla \cdot (M_{\text{CH}_4} \vec{u}_f) + R_{\text{CH}_4} \quad (17)$$

where  $M_{\text{CH}_4}$  is the mass of methane per unit area. Note that the pore velocity  $\vec{u}_f = \vec{v}_f / \phi$  rather than the Darcy velocity  $\vec{v}_f$  appears in equation (17). We use the finite volume method on the unstructured triangular finite element meshes (e.g., Vehling et al., 2018) to accumulate and advect methane until it is possibly released by hydrothermal venting at the top. We have benchmarked our implementation of sill cooling/crystallization, organic cracking, and dehydration against data from contact aureoles around a 10.4-m-thick dike (see supporting information S1).

### 3.4. Magma Crystallization

The crystal fraction  $\phi_C$  in the cooling sill is described as a simple, linear function of temperature between liquidus temperature  $T_L$ , and solidus temperature  $T_S$ . For  $T_S \leq T \leq T_L$ , we define

$$\phi_C = 1 - \left( \frac{T - T_S}{T_L - T_S} \right) \quad (18)$$

The rate of magma crystallization,  $R_C$ , is given by

$$R_C = \rho_r \frac{\partial \phi_C}{\partial t} \quad (19)$$

We do not consider physical or thermodynamic changes of the magma during crystallization so that all sill properties remain constant (see Table 1). Furthermore, the magma is assumed to have zero pore space and to be impermeable so that hydrothermal circulation cannot penetrate the sill.

### 3.5. Mohr-Coulomb Rheology, Hydrofracturing, and Dynamic Permeability

Saucer-shaped sills develop in comparatively strong host-rock environments and cause an uplift of the elastically deforming overburden. As a result of this deformation, a stress anomaly exists in the overburden above the edges of the saucer-shaped sill (cf. section 1 and Figures 1B and 1C). When pore pressure increases, rocks fracture once a critical yield pressure is exceeded; a process called hydrofracturing. The fractured rock will have a higher permeability, which in turn may affect the flow paths and time scales of the hydrothermal system. Already-stressed rocks require a lower critical pressure to initiate failure, which we take into consideration in our models with saucer-shaped sills. In our model, we formulate a Mohr-Coulomb failure criterion

$$\tau = \sigma_n \cdot \tan(\theta) + C \quad (20)$$

where  $\tau$  is the shear strength,  $\sigma_n$  is the normal stress,  $C$  is the rock's cohesion, and  $\theta$  is the angle of internal friction. Failure occurs when the Mohr-Circle touches or exceeds the failure envelope. For any given stress state, the tangential point of the Mohr-Circle to the failure envelope defines the critical stress required for failure. We consider both shear failure mode derived here to explicitly include the differential stress

$$F_{\text{shear}} = \sigma_m - \frac{\sigma_{\text{diff}}}{2} \cdot \sin(\theta) \quad (21)$$

and tensile failure mode

$$F_{\text{tensile}} = \left[ \sigma_m - \frac{\sigma_{\text{diff}}}{2} \cdot \sin(\theta) \right] \cdot \tan(\theta) + C \quad (22)$$

where  $\sigma_m = \frac{(\sigma_1 + \sigma_3)}{2}$  is the mean stress,  $\sigma_{\text{diff}} = \sigma_1 - \sigma_3$  is the differential stress, and  $\sigma_1$  and  $\sigma_3$  are the largest and smallest principle stresses, respectively. We assume that the vertical load is the largest principle stress (i.e.,  $\sigma_1 = \sigma_z$ ), while the horizontal stress is the smallest principle stress. The latter is defined to be a fraction  $A$  of the vertical load, that is,  $\sigma_3 = \sigma_x = A \sigma_z$ . For flat sills emplaced in shale lithologies without uplifting the overburden, we use  $A = 1$ , so that the differential stress is 0 everywhere. Saucer-shaped sills emplaced in sandstone lithologies are assumed to have uplifted the overburden. Here we choose a Gaussian-shaped transition from  $A = 0.7$  to  $A = 1$  in a 1.5-km-wide vertical column above the sill edges up to the surface and  $A = 1$

everywhere else (see supporting information S1). Failure occurs where the pore fluid pressure exceeds the pressure required for failure, that is,

$$P \geq P_{\text{fail}} = \min[F_{\text{shear}}, F_{\text{tensile}}] \quad (23)$$

The above formulation defines the conditions for hydraulic fracturing of the permeable host-rock. Permeability increase accompanies mechanical failure because fractured rock provides more permeable pathway for penetrating fluids. This increase in permeability upon failure, especially the dynamic feedback between pore pressure, mechanical failure, and permeability changes, has been found to affect the tempo-spatial evolution of hydrothermal systems (e.g., Weis, 2015). To quantify the local increase of permeability during failure, we follow the formulation given by Weis (2015), which uses the ratio  $\lambda$  between actual pore pressure and the pressure required for failure

$$\lambda = \frac{P}{P_{\text{fail}}} \quad (24)$$

In regions, where failure occurs (that is,  $\lambda > 1$ ), we increase the porosity-controlled permeability  $K(\phi)$  for the next time step according to

$$K(\phi, P) = K(\phi) \cdot \min[\lambda^a, 100] \quad (25)$$

where the exponent  $a = 2$  is used to scale the permeability increase. We limit the maximum permeability increase from hydrofracturing to 2 orders of magnitude above the initial permeability. Note that the failure-related permeability increase defined by equation (25) is assumed to be reversible so that permeability returns to its porosity-controlled value  $K(\phi)$  once pore pressure drops again below the failure pressure.

### 3.6. Brittle-Ductile Transition

The above hydromechanical processes are largely controlled by temperature and also occur in the contact aureole of the sills, where temperatures reach several hundred degrees Celsius after the sill emplacement. Above a certain temperature, sedimentary rocks change their deformation behavior from brittle to ductile, which affects the Mohr-Coulomb rheology introduced above. We include the effect of this brittle-ductile transition by modifying the differential stress  $\sigma_{\text{diff}}$  at higher temperatures. We assume the brittle-ductile transition occurs between  $T_{\text{brittle}} = 500$  °C and  $T_{\text{ductile}} = 750$  °C, where the latter is the estimated melting temperature of a sedimentary rock (e.g., Aarnes et al., 2010; Nichols et al., 1994). Within this temperature range, we reduce the differential stress linearly according to

$$\sigma_{\text{diff}} = \sigma_{\text{diff}} \cdot \left( 1 - \frac{T - T_{\text{brittle}}}{T_{\text{ductile}} - T_{\text{brittle}}} \right) \quad (26)$$

Above 750 °C, the rocks are assumed to behave perfectly ductile and to have a zero differential stress.

### 3.7. Model Initialization and Boundary Conditions

We assume that the Karoo Basin temperature distribution was at steady state at the time of the Karoo LIP emplacement. For our initial temperature, we use the average heat flow of the Namaqua-Natal basement of  $61 \pm 11$  mW/m<sup>2</sup> (Jones, 1993) and solve for the steady state geothermal gradient considering the stratigraphic profile used in the calculation. The resulting geothermal gradient of about 25.3 °C/km is consistent with Jones (1993) and Dhansay et al. (2017).

All simulations assume an instantaneous emplacement of the magmatic body with an initial temperature of 1150 °C, which is also the assumed liquidus temperature. The sills are defined to have zero porosity throughout the simulations and are hence impermeable (cf. equation (11)). All sills have a thickness of 100 m and a horizontal extent of 6.4 km. After emplacement, each sill cools dynamically in response to conductive heat loss to the surrounding rock and heat removed by hydrothermal fluid flow.

The boundary conditions of all model calculations are as follows. Side boundaries and bottom are impermeable and thermally insulating, while the top boundary mimics an ocean floor where fluids are allowed to enter and leave the domain. Here we use a mixed boundary condition (e.g., Hasenclever et al., 2014),

where fluids enter at 2 °C at inflow locations and vent freely with  $\frac{\partial T}{\partial z} = 0$  at outflow locations. Pressure at the top is fixed at 25 MPa. We run all calculations until fluid flow velocity become very low and only heat conduction occurs within the domain, which occurred after 100,000–250,000 years depending on the model setup.

## 4. Application to the Karoo Basin, South Africa

### 4.1. General Setup

In order to apply our model to the Karoo Basin some simplifications have been made. The Karoo Basin stratigraphy can be summarized as a succession of sandstone-dominated formations (of the Stormberg Gp. and Beaufort Gp.) from the basin top down to almost the deepest formation, which is dominantly made of organic-rich shale formations (Ecca Gp.). Using this basic stratigraphic sequence, we have dissected the basin in three regions with different basin depths (Figure 2). Each of these regions will be investigated in a specific 2-D modeling section, which we refer to as setups S1, S2, and S3. In each of these setups, sills and saucer-shaped sills are placed according to the basic relation identified above, which relates host-rock accommodation process and sill geometry (i.e., saucer-shaped sill in sandstone lithology and flat-lying sill in shale lithology, Figure 2B).

This procedure leads to a first-order approximation of the Karoo Basin sediment volume. Using the Karoo Basin sediment thickness estimates from the Laske et al. (2013) database, we have calculated the area of the basin where sediment depth was ranging between the surface down to 1.2 km, that is, 309,928 km<sup>2</sup>; 1.2 to 2.9 km, that is, 137,752 km<sup>2</sup>, and 2.9 to 5.7 km, that is, 55,036 km<sup>2</sup>. These regions are further used to estimate a corresponding volume of sedimentary rock associated with each setup, S1: 371,913 km<sup>3</sup>, S2: 399,482 km<sup>3</sup>, and S3: 313,708 km<sup>3</sup>. These volumes will be used in our quantitative estimate of the thermogenic degassing associated with the Karoo LIP plumbing system.

The conducted 2-D simulations have the objectives to (1) determine the amount of degassing at the basin top and (2) establish the time lapse between magma emplacement at depth and degassing at the basin top. The numerical setups considered in this study are summarized in Table 2 and illustrated in Figure 2B. The general vertical distribution of sill intrusions along our synthetic stratigraphic log is based on a statistical distribution of sills found in 27 boreholes across the Karoo Basin (Svensen et al., 2018, supporting information S1). Details of distribution and thickness of the sills in the Ecca Gp. and Beaufort Gp. is based on previous studies (Aarnes et al., 2011; Galerne et al., 2008) and include field observations, geological mapping (Johnson et al., 1996), and satellite images. Based on borehole data published by Svensen et al., (2018), we have calculated that 23% of the Beaufort Gp. and Ecca Gp. consist of sill intrusions (supporting information S1). This value is consistent with a previous estimate of sill to sediment proportion in the Karoo Basin (Rowse & De Swardt, 1976). To reflect this information in our quantitative estimate of thermogenic gas mobilization and degassing at basin scale, the thinnest setup S1 only contains two levels of saucer-shaped sills in the Beaufort Gp. and one level of flat sills in the Ecca Gp., while setups S2 and S3 each contain three levels of saucer-shaped sills in the Beaufort Gp. and two levels of flat sills in the Ecca Gp. (Figure 2B).

### 4.2. One-Dimensional Reference Profile

Our one-dimensional reference lithostratigraphic profile (Figure 2C) represents the thickest part of the basin (S3 in Figure 2B) and combines information from boreholes (Svensen et al., 2018) and stratigraphic studies (Catuneanu et al., 1998; Johnson et al., 2006; Campbell et al., 2016, Campbell et al., 2016). It provides basic depth changes in lithology that lead to variations in material properties (Figure 2C). For simplification, we have assumed that the formation thicknesses for the smaller setups S2 and S1 decrease linearly in proportion to each section's depth, using S3 as reference.

To construct the porosity profile (Figure 2C), we use data of a recent study that systematically reports the porosity variation of each successive formation in the Karoo (Baiyegunhi et al., 2014). We consider them as reference surface porosity values ( $\phi_0$ ) for each formation in our depth-dependent porosity equation (equation (10)). Although porosity might have changed over time, for example, through processes like cementation, this procedure enables us to respect the relative variations in porosity from one formation to the next. This porosity profile is then used in the simplified Kozeny-Carman equation (equation (11)) to calculate a permeability-depth profile. For comparison, we show our calculated porosity and permeability profiles

**Table 2**  
Summary of the 13 Setups That Are Relevant for the Karoo Basin

Stratigraphic Group	Host rock	Sill		Setup 1 (S1)			Setup 2 (S2)			Setup 3 (S3)			
		Geometry	Level	Depth (km)	TOC (wt.%)	Name	Depth (km)	TOC (wt.%)	Name	Depth (km)	TOC (wt.%)	Name	
Stormberg	Sandstone	No sills <sup>a</sup>	—	—	—	—	—	—	—	—	—	—	
Beaufort	Sandstone	Saucer	Level 3 (top)	—	—	—	0.6	0.5	S2-B3	1.2	0.5	S3-B3	
			Level 2 (middle)	2	0.4	0.5	S1-B2	1.0	0.5	S2-B2	2.0	0.5	S3-B2
			Level 1 (lower)	1	0.8	1.0	S1-B1	1.7	1.0	S2-B1	3.4	1.0	S3-B1
Ecca	Shale	Flat sill	Level 2 (top)	—	—	—	2.4	2.8	S2-E2	4.7	2.8	S3-E2	
			Level 1 (lower)	1	1.0	4.5	S1-E1	2.6	4.5	S2-E1	5.1	4.5	S3-E1
Dwyka	Diamictite	No sills <sup>a</sup>	—	—	—	—	—	—	—	—	—	—	

*Note.* This table supports Figure 2.B starting with the stratigraphy on the left, followed by sill geometry and depth levels. The depth of the sill levels is specific to each setup. Note that consistent with field observations, the Stormberg Group do not host any major sills (e.g., Chevallier & Woodford, 1999). Each sill in our simulations are considered to have a thickness of 100 m, the most common thickness considered for the Karoo sills (e.g., Aarnes et al., 2010; Iyer et al., 2013). TOC = total organic carbon.

<sup>a</sup>Few sills may be found across the Karoo Basin in the Stormberg Group and Dwyka Group; however, they are scarce and not taken into consideration in our quantitative estimates (e.g., Chevallier & Woodford, 1999).

and the porosity/permeability range measured by Campbell, Lenhardt, et al. (2016) for the Ripon Formation (see blue bars, Figures 2C2 and C3).

The initial weight percent TOC profile (Figure 2C) is compiled from various sources (EIA, 2015; Branch et al., 2007; Faure & Cole, 1999). Although the Whitehill Formation has reported values as high as 15- to 17-wt.% TOC (Branch et al., 2007; Faure & Cole, 1999) we chose a mean value of 4.5-wt.% TOC as representative of the average TOC content of the formation at basin scale. Finally, the thermal conductivity and heat capacity of the reference lithostratigraphic profile (Figure 2C) is constructed from mixed end-member values (Čermák & Rybach, 1982) corresponding to the main rock type associated with each sedimentary formation (e.g., Catuneanu et al., 1998; Johnson et al., 2006).

## 5. Results

### 5.1. A Dynamic Porosity/Permeability Model

Our model calculations take into account the dynamic changes in porosity and permeability that evolve over time as the result of the thermomechanical processes and reactions described above. To demonstrate the impact of the sill geometry, dehydration, and hydraulic fracturing on the hydrothermal fluid flow, we have performed five reference simulations in simplified setups (named S0 in Table 3; see supporting information S1 for the specificity of each setup). These simulations assume homogeneous material properties of the host-rock throughout the domain (i.e., constant density, thermal conductivity, heat capacity, thermal conductivity, and TOC) and a gradual depth variation in porosity and permeability (see black curves in Figure 2C). In Figure 3, we compare the model evolution after 30 years for flat-lying sills and saucer-shaped sills with and without hydrofracturing. In addition, we show a saucer-shaped sill with preexisting differential stress in the overburden and hydrofracturing (see Figure 3 and Table S2.1 in supporting information S2).

Two mechanisms induce changes in permeability: Host-rock dehydration represents a mass transfer from the host-rock to the fluid that leads to an irreversible increase in porosity and hence permeability. Regions where this occurs are outlined by gray contours in Figure 3. Not only in the contact aureole but also in the ~400 °C hot hydrothermal plumes temperatures are sufficiently high to trigger the dehydration reaction (Figure 3, column 1 and column 2). The resulting pattern shows complete dehydration in the vicinity of the sill and ~50% dehydration along the pathways of rising thermal plumes (Figure 3).

The second mechanism affecting permeability is related to mechanical failure of the host-rock in regions where the pore pressure exceeds the yield strength of the rock. In contrast to the host-rock dehydration, this process induces a temporary permeability increase. This simulates the process of fracture opening at high

**Table 3**

*Report of Maximum Venting Temperature and Surface Degassing as well as Integrated Thermogenic Methane Gas Mobilization, Surface Flux Emissions, and Stalled on the Way to the Surface (for Methane Only) at the End of the Hydrothermal Fluid Flow*

Setup	Depth (km)	TOC (wt.%)	Maximum surface temperature (°C)	At year	Maximum methane degassing flux (kg/year)	At year	End of the hydrothermal fluid flow (kyr)
S0-1a	1.0	5.0	244	209	202,156	190	100
S0-1b	1.0	5.0	136	606	85,730	427	100
S0-2a	1.0	5.0	388	88	530,429	101	100
S0-2b	1.0	5.0	302	145	455,463	85	100
S0-3	1.0	5.0	309	303	414,961	69	100
S1-B2	0.4	0.5	400	76	51,956	82	60
S1-B1	0.8	1.0	173	506	23,561	325	80
S1-E1	1.1	4.5	48	4,567	290	9,467	100
S2-B3	0.6	0.5	388	106	40,243	39	160
S2-B2	1.0	0.5	92	1,341	3,065	911	180
S2-B1	1.7	1.0	31	10,025	0	33,875	200
S2-E2	2.4	2.8	35	21,116	16	98,216	250
S2-E1	2.6	4.5	29	56,636	12	101,344	250
S3-B3	1.2	0.5	54	3,057	866	2,627	190
S3-B2	2.0	0.5	36	17,509	0	100,064	220
S3-B1	3.4	1.0	46	56,251	1	55,351	250
S3-E2	4.7	2.8	15	18,146	0	14,246	250
S3-E1	5.1	4.5	11	8,394	0	3,151	250

Percentages Are Normalized to Mobilized Values Obtained in Each Setup

Setup	Depth (km)	TOC (wt.%)	Mass (ton)					Percentage (%)			
			Mobilized		Emitted		Stalled	Emitted		Stalled	Total CH <sub>4</sub>
			H <sub>2</sub> O	CH <sub>4</sub>	H <sub>2</sub> O	CH <sub>4</sub>	CH <sub>4</sub>	H <sub>2</sub> O	CH <sub>4</sub>	CH <sub>4</sub>	
S0-1a	1.0	5.0	132,083	369,832	1,637,313	213,447	106,275	8	58	29	86
S0-1b	1.0	5.0	105,152	319,373	1,414,868	165,467	95,302	7	52	30	82
S0-2a	1.0	5.0	133,756	359,194	1,690,051	225,887	91,026	8	63	25	88
S0-2b	1.0	5.0	112,394	315,269	1,422,776	184,304	78,404	8	58	25	83
S0-3	1.0	5.0	110,031	310,508	1,410,851	188,103	65,292	8	61	21	82
S1-B2	0.4	0.5	83,239	24,898	446,992	6,505	5,179	19	26	21	47
S1-B1	0.8	1.0	95,221	58,508	532,658	19,055	17,806	18	33	30	63
S1-E1	1.0	4.5	98,340	77,169	505,853	5,533	61,818	19	7	80	87
S2-B3	0.6	0.5	94,377	40,809	659,977	7,513	6,177	14	18	15	34
S2-B2	1.0	0.5	100,163	59,149	568,207	8,450	14,518	18	14	25	39
S2-B1	1.7	1.0	96,485	81,612	453,592	7	33,375	21	0	41	41
S2-E2	2.4	2.8	115,481	162,072	931,329	814	120,871	12	1	75	75
S2-E1	2.6	4.5	127,439	165,647	1,012,539	792	158,215	13	0	96	96
S3-B3	1.2	0.5	104,266	43,329	604,562	5,036	16,402	17	12	38	49
S3-B2	2.0	0.5	108,795	50,313	553,253	13	29,773	20	0	59	59
S3-B1	3.4	1.0	124,915	85,754	601,591	17	56,327	21	0	66	66
S3-E2	4.7	2.8	148,258	271,110	542,080	0	205,401	27	0	76	76
S3-E1	5.1	4.5	141,491	337,789	586,944	0	290,396	24	0	86	86

Note. TOC = total organic carbon.

pore fluid pressures and closing again after pore pressure has dropped. Regions where hydrofracturing occurs are outlined by white contours in Figure 3. As discussed above, saucer-shaped sills emplaced in sandstone lithology cause a deformation of the overburden. The reference simulation S0-3 (Figure 3E) assumes an associated preexisting differential stress above the edges of the saucer (Figure 3E4). The prestressed rock facilitates hydrofracturing because the pore pressure required for failure is lower. A vertically elongated hydrofractured region extends above the rising thermal plume toward the surface (Figure 3E). As a result, the thermal plume propagates faster toward the surface and forms a narrower upflow zone (see Figure 3E1 and supporting information Figure B3).

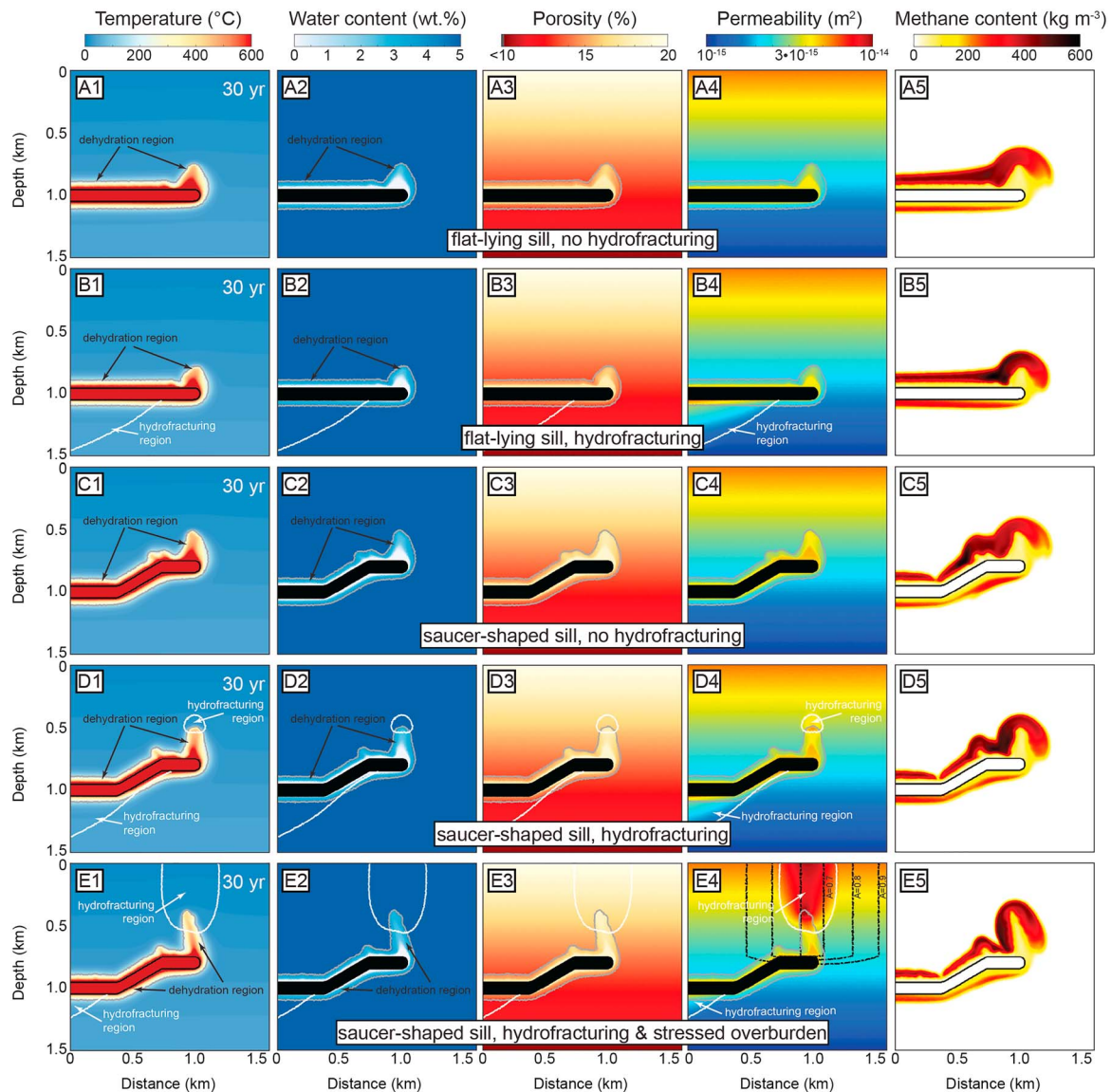


**Figure 3.** The effect of dehydration and hydrofracturing process on hydrothermal fluid flow pattern for different sill geometries (A, B: flat-lying sill; C–E: saucer-shaped sill), hydrofracturing process disabled (A, C) or enabled (B, D, E), as well as prestressed overburden (E). Column 1: temperature, Column 2: water content, Column 3: porosity, Column 4: permeability, and Column 5: methane content of fluid. All results are shown after 30 years of cooling. To visualize the evolution in time the same figure is displayed after 70 years in supporting information S1 (Figure S2.2). Black contour line in E4 mark the ratio of principal stresses  $\sigma_3/\sigma_1$ , which we use to parametrize the overburden stress state.

These different processes have consequences for the hydrothermal fluid flow and the transport of methane (Figure 3, column 5). All setups show that the first and strongest hydrothermal plumes form above the sill edges, where heated fluid from above and below the sill merge to form a strong upflow. However, saucer-shaped sills establish in addition a strong flow along their inclined part and toward the edges. The resulting thermal plumes are stronger than those above flat-lying sills and cause higher pore pressures in the host-rock at the front of these rising plumes (Figures 3D and 3E). These high pressures facilitate hydrofracturing (outlined by white contours, Figures 3D and 3E). If the host-rock is prestressed, these regions extend to the surface (Figure 3E).

### 5.2. High-Permeability Channels and Venting Efficiency

High-permeability channels promote a faster flow of the hydrothermal fluids and are a very efficient pathway for methane released within the contact aureole toward the vent sites. Note that the first methane

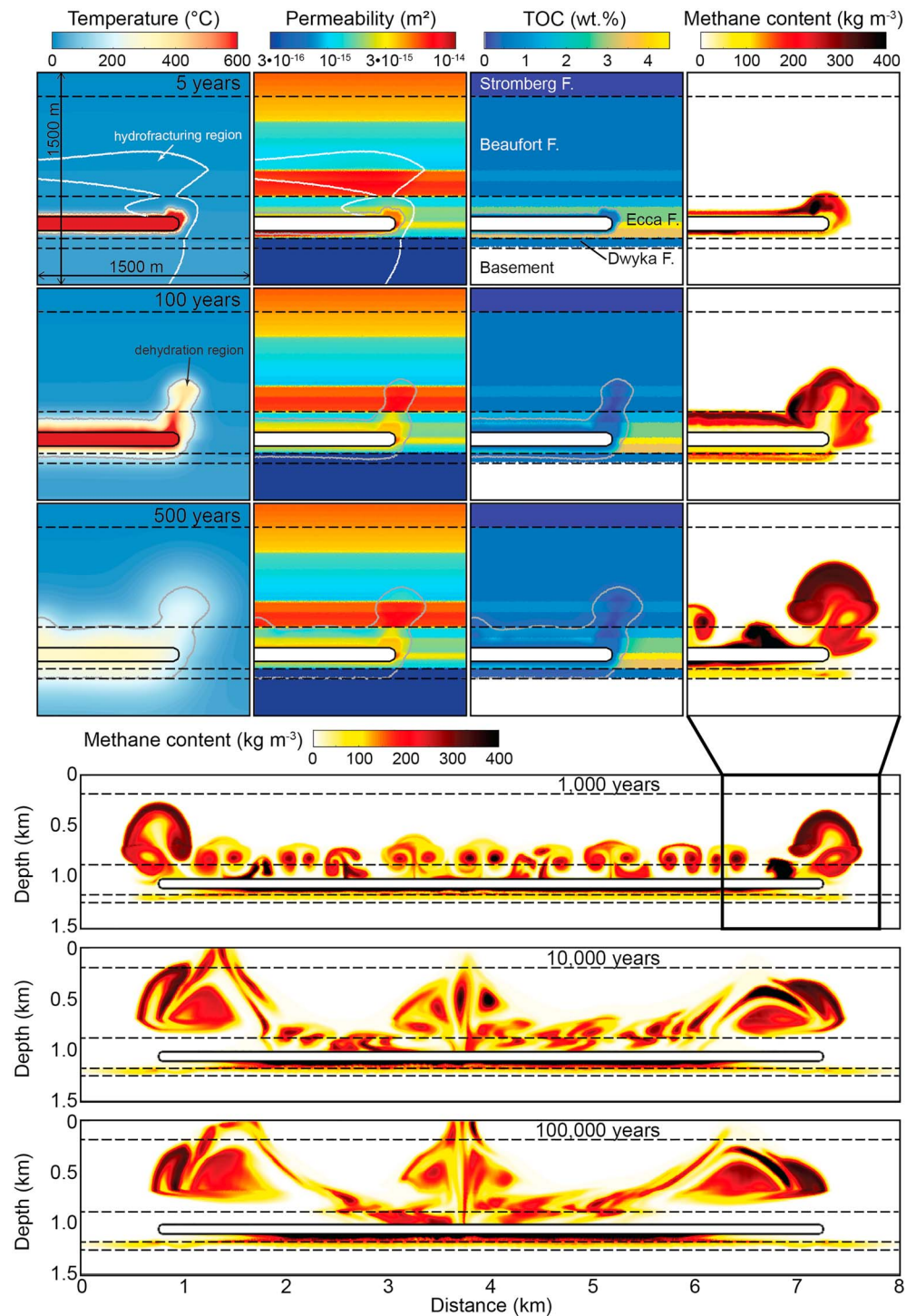


**Figure 4.** Time evolution of setup S1-E1 between 5 years and 100,000 years: A flat-lying sill emplaced in the organic-rich Ecca formation. The first 500 years illustrate how temperature (first column), permeability (second column), total organic carbon (TOC, third column), and methane content (fourth column) evolve during the hydrothermal fluid flow. The evolution of the methane content and its transport to the surface is shown for the whole sill at 1,000, 10,000, and 100,000 years.



bearing fluids that arrive at the surface are cold (white contour line in Figure 3, column 5 marks the 50 °C isotherm). These fluids were initially next to the sill. During their ascent, they heated up the host-rock that they percolated through. As consequence, these fluids are cold yet carry high concentrations of methane. After the host-rock is heated up along the hydrothermal fluid path, venting temperatures increase. The maximum venting temperatures in the five reference setups are summarized in Table 3. We observe that independent of the sill geometry, maximum surface temperature decreases when hydrofracturing and the associated permeability increase are accounted for. The high-permeability channel not only accelerates the ascent of the thermal plume but also facilitates mixing between hydrothermal fluid and cold subsurface water—a process described in detail in Andersen et al. (2015). The end result is a maximum surface temperature difference of ~80 °C for the reference simulations with saucer-shaped sills (S0-2a, S0-2b, and S0-3, Table 3) and almost 110 °C for the flat-lying sills (S0-1a and S0-1b, Table 3). Similarly, maximum degassing rates slightly decrease when hydrofracturing is accounted for (Table 3), which we also explain by enhanced mixing between methane-bearing hydrothermal fluids and methane-free subsurface water. Furthermore, simulations without hydrofracturing reach their maximum vent temperature and maximum degassing rates earlier than those with hydrofracturing (Table 3).

Our result shows that dehydration alone (S0-1a and S0-2a) is a more efficient process at transporting and emitting thermogenic methane to the basin floor. The fraction emitted compared to the amount mobilized at depth by thermal cracking is of 58% for the flat-lying sill case and 63% for the saucer-shaped sill case (S0-1a and S0-2a, respectively, Table 3). Introducing hydrofracturing reduces these fractions to 52% (S0-1b, flat-lying sill, Table 3) and 58% (S0-2b, saucer-shaped sill, Table 3). Finally, acknowledging the prestressed overburden above the saucer-shaped sill edges result in a 61% emitted fraction at the ocean floor (S0-3, Table 3). Because dehydration is at the heart of our novel model, it is difficult to compare to previous published models that did not account for the effect of porosity and permeability increase upon dehydration (e.g., Iyer et al., 2013). Although, our model seems to decrease the amount of thermogenic methane emitted at the basin floor (by a couple of fractions), our model considerably amplify the degassing rates at the basin floor. After only 3,000 years, all reference simulations with saucer-shaped sills have emitted at least 35% of the mobilized thermogenic methane and more than 50% after 20,000 years. For comparison, only 10% of the mobilized thermogenic gas is emitted to the surface after 34,000 years if no porosity evolution and hydrofracturing processes are considered (Iyer et al., 2013).

### 5.3. Models Calculations for the Karoo Basin

#### 5.3.1. Impact of the Stratigraphy and Sill Geometry

To illustrate the impact of the stratigraphy and the above mechanical/hydrothermal processes, we report results of two scenarios: S1-E1 and S2-B2 (Table 2). The first scenario (S1-E1) corresponds to a flat-lying sill emplaced at 1-km depth into a shale-dominated lithology. Consistent with the viscous indenter accommodation process (Figure 1B), no differential stress is considered in the overburden. However, compared to sandstone, shale lithologies have greater cohesion and a lower internal angle of friction (Table 1). These rheological properties considerably reduce the required pressure for failure upon pore pressure increase. The result is a broad failure pattern around the cooling sill (white contours in Figure 4, time: 5 years), which disappears rapidly with the relatively fast pore pressure dissipation. After few years, only the permeability increase associated with host-rock dehydration is present. After 100 years, the progressing methane plumes enter a sandstone lithology with lower permeability (Figure 4, time 100–500 years), which slows down the ascent. At about the same time, the front of thermal plume cools to temperatures below ~250 °C and host-rock dehydration stops at about 600 m below the surface. Hydrothermal cooling over time leaves the central part of the sill as the only high-temperature region. The resulting broad upflow, central above the sill, drives methane charged fluids toward the center and upward so that the main degassing location lies central. In particular, deeper flat-lying sills (setups S2-E1 and S2-E2) show this kind of pattern. Due to its relatively shallow depth of 1 km, the illustrated setup S1-E1 has three degassing locations (Figure 4, 100,000 years).

The second scenario (S2-B2) corresponds to a saucer-shaped sill emplaced at 1-km depth into sandstone dominated lithology. Consistent with the forced fold mechanism (Figure 1B), the differential stress localized above the tips of the saucer-shaped sill favors hydrofracturing and the formation of high-permeability zones above both ends of the saucer (Figure 5, 5 years). Supported by flow up the slope near the edge of the saucer,

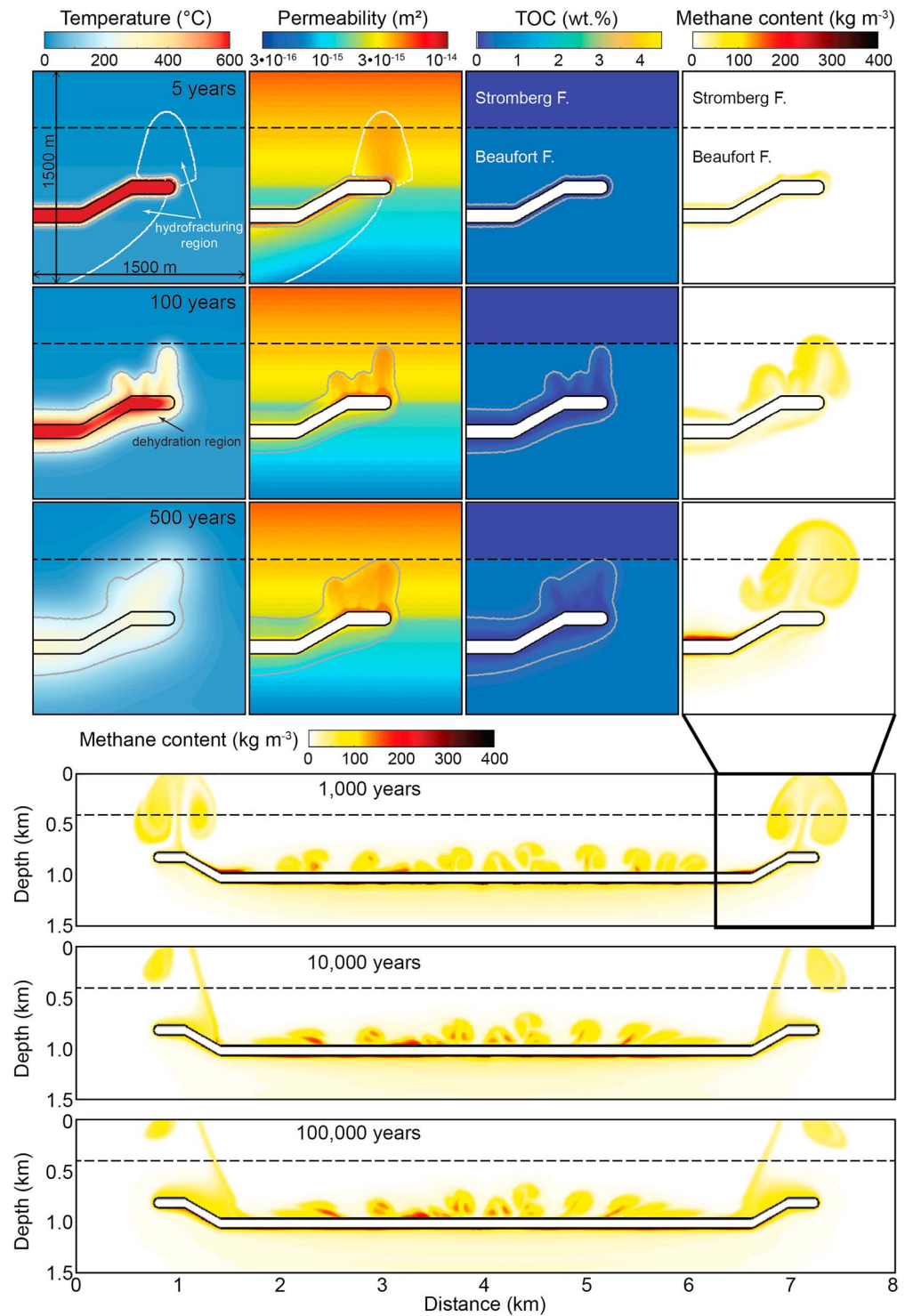


**Figure 5.** Time evolution of setup S2-B2 between 5 years and 100,000 years: A saucer-shaped sill emplaced in the less organic-rich Beaufort formation. See Figure 4 for complementary caption and text for details. TOC = total organic carbon.

thermal plumes quickly develop and progress toward the surface. Failure associated with excess pore pressure vanishes around the inclined edges of the saucer within ~15 years. Methane degassing starts about 700 years after sill emplacement, and over a period of 100,000 years, the two main methane plumes at the saucer ends have released most of their methane to the surface (Figure 5, time 100,000 years). This

result contrasts with the flat-lying sill scenario that shows a later onset of methane degassing at  $\sim 7,000$  years at a location central above the sill (Figure 4).

### 5.3.2. Flow Patterns and Venting Locations

The two scenarios reported above (S1-E1, Figure 4; S2-B2, Figure 5) well illustrate the contrasting behaviour of the hydrothermal systems associated with a saucer-shaped sill and a flat-lying sill. In the case of a saucer-shaped sill, the fluid flow is preferentially guided into two vertical channels developing at the ends of the saucer. This flow pattern remains relatively fixed over time (Figure 5). The high fluid temperatures cause host-rock dehydration along these vertical paths and form persisting high-porosity, high-permeability channels that promote early high-temperature venting. In case of very shallow saucer-shaped sills, these dehydration channels reach the surface (S1-B2 and S2-B3, see Table 3). The two main high-temperature venting locations are located above the rim of the saucer (Figure 5). In contrast, flat-lying sills trigger a more complex fluid flow pattern above the sill that changes through time (Figure 4). As time progresses, the hydrothermal upflow zone migrates from the edges toward the sill center where the remaining thermal energy is located. Methane-bearing fluids migrate toward the center of the sill to finally vent at the surface (Figure 4). If the sill is deep enough, that is,  $>1$  km, only the central venting location forms while vent locations above the sill's edges are absent.

### 5.3.3. Venting Temperature and Thermogenic Degassing

Our results show that the main temperature signal recorded at the surface of the modeled basin is characterized by an early high-temperature event (within the first few thousand years, Table 3 and Figure 6A) corresponding to the arrival of thermal plumes generated at the ends of the simulated sills. The events with highest vent temperatures are associated with saucer-shaped sills and range from  $\sim 55$  °C up to  $\sim 400$  °C (S1-B1, S1-B2, S2-B2, S2-B3, and S3-B3, Table 3 and Figure 6). For these setups maximum temperatures and degassing rates gradually increase toward shallower emplacement depths (particularly in the last 1.5 km; Table 3). Most of the deeper flat-lying sills show only a very weak temperature signal of  $<50$  °C, which does persist for a much longer time than the high-temperature signal of shallower saucer-shaped sills (e.g., S2E1 compared to S2B2 and S1B1, Figure 6B). Although less obvious, a surface temperature to depth trend also exists for flat-lying sills. Surface venting onset characterized by peak surface temperatures and high degassing rates in stratified simulations, occurs almost simultaneously for shallow sills (Figure 6A). However, temperature rapidly decreases below 50 °C, while degassing rates remain significant for a longer period (e.g., S1-B1, S1-E1, and S2-B2, Figure 6). Finally, we observed that sills shallower than 1.5 km (mostly saucer-shaped sills in the case of the Karoo Basin) display a relative synchronicity of their peak surface temperature and maximum degassing rates (Figure 6B).

A second type of heat signal is characterized by a considerable time delay in arriving to the surface. It corresponds to flat sills deeper than 1 km and saucer-shaped sills deeper than 1.7 km. The maximum temperatures associated with these events are generally low, ranging from between  $\sim 25$ – $35$  °C for the saucer-shaped sills (S2-B1, S3-B1, and S3-B2, Table 3) and between  $\sim 30$ – $50$  °C for the flat-lying sills (S1-E1, S2-E1, S2-E2, and S3-E1, Table 3 and Figure 6). Maximum surface venting temperature for these setups occur after 10,000 years (Table 3 and Figure 6B). Note that the only setup showing any significant surface degassing among these is S1-E1.

## 5.4. Quantification of In Situ Mobilization and Surface Degassing

The end of the hydrothermal fluid flow can be identified as the time when fluid flow velocities become very low and only heat conduction occurs within the domain. At this time, the transient heat source anomaly associated with the cooling sill has become too small to drive hydrothermal flow. Due to the various sill depths considered, ambient geothermal gradient varies from one setup to the next so that the end of the hydrothermal activity is specific to each setup (Table 3) and is represented by the end of the colored bars in Figure 6.

Here we report quantitative amounts of water and thermogenic methane mobilized by dehydration and organic cracking, respectively, and emitted during the hydrothermal activity. We also report the amount of methane stalling on the way to the surface at the end of the hydrothermal fluid flow.

For all setups, we observe an increase in mobilized water with sill emplacement depth (Figure 7 and Table 3). This trend is explained by the geothermal gradient that leads to higher ambient temperatures at greater depths, so that host-rocks are already closer to the dehydration window and less additional heat from the sill is required to trigger dehydration. The deepest flat-lying sills are emplaced only a few

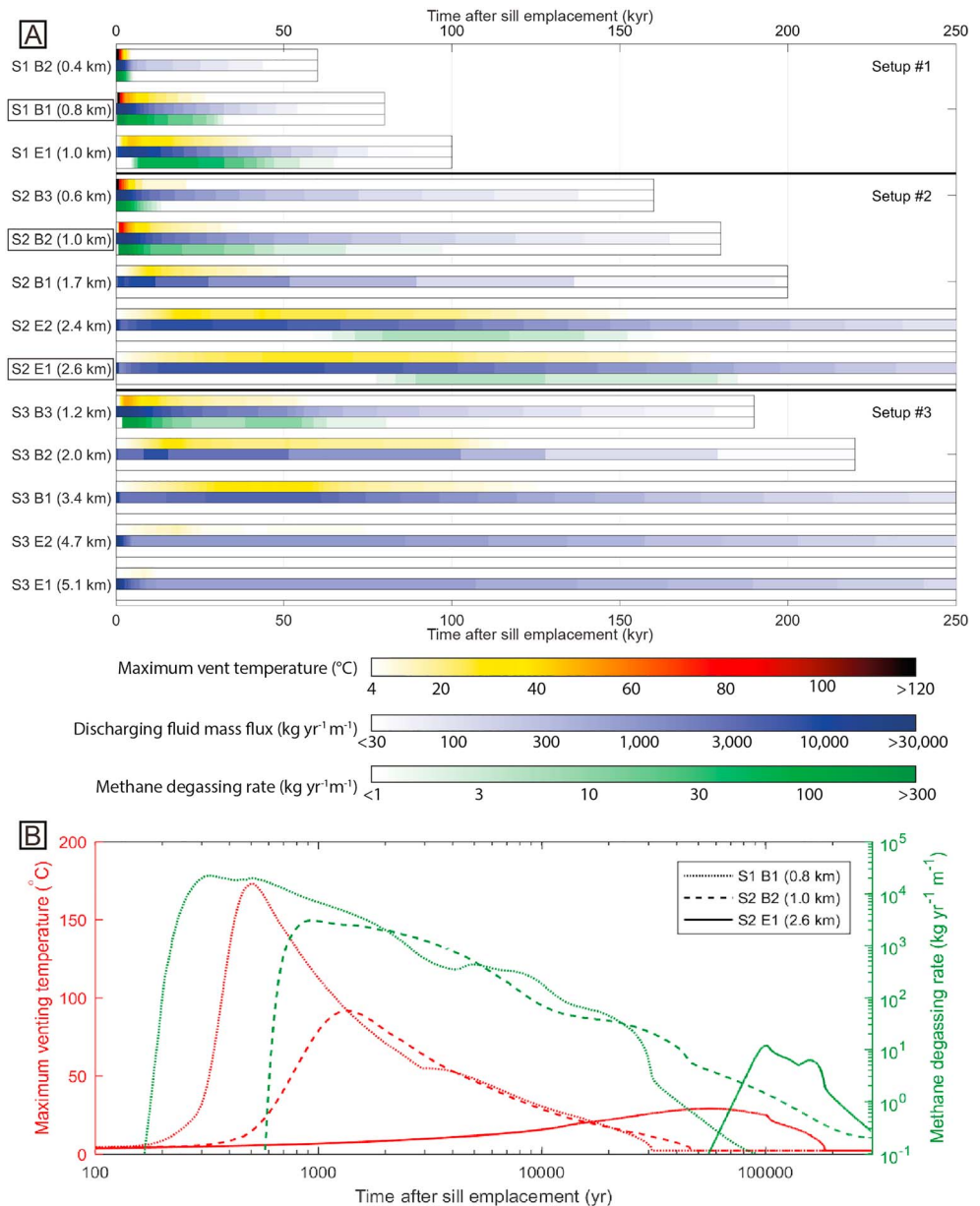


**Figure 6.** (A) Summary of venting temperature and surface degassing of all setups that include stratigraphic information on the Karoo basin. For each setup, we show, as a function of time, highest temperature of the venting fluids (upper bar in each block), mass flux of the discharging water (middle bar), and mass flux of the degassing methane (lower bar). The depth of each sill is given in the labels on the left side. (B) Evolution of the maximum venting temperature and methane degassing rate over time for S1-B1, S2-B2, and S2-E1. See text for details.

hundred meters above the impermeable basement through which heat is only conducted away from the sills. This has an insulating effect and leads to somewhat higher temperatures in the host-rocks sandwiched between the sills and the basement. The amount of water emitted at the surface ranges, for all setups, from ~450 to ~650 kt (Figure 7). The only two exceptions are the flat-lying sills of the setup S2. These setups, S2-E1 and S2-E2, typically display the insulating effect described above and have therefore an extended duration of hydrothermal activity that is reflected in the total amount of water emitted at the surface of the domain (up to 1,000 kt, Figure 7).

The initial TOC content of the host-rock is an important factor controlling the amount of material that can be potentially mobilized and emitted at the basin top. Our model calculations consider the Karoo Basin TOC

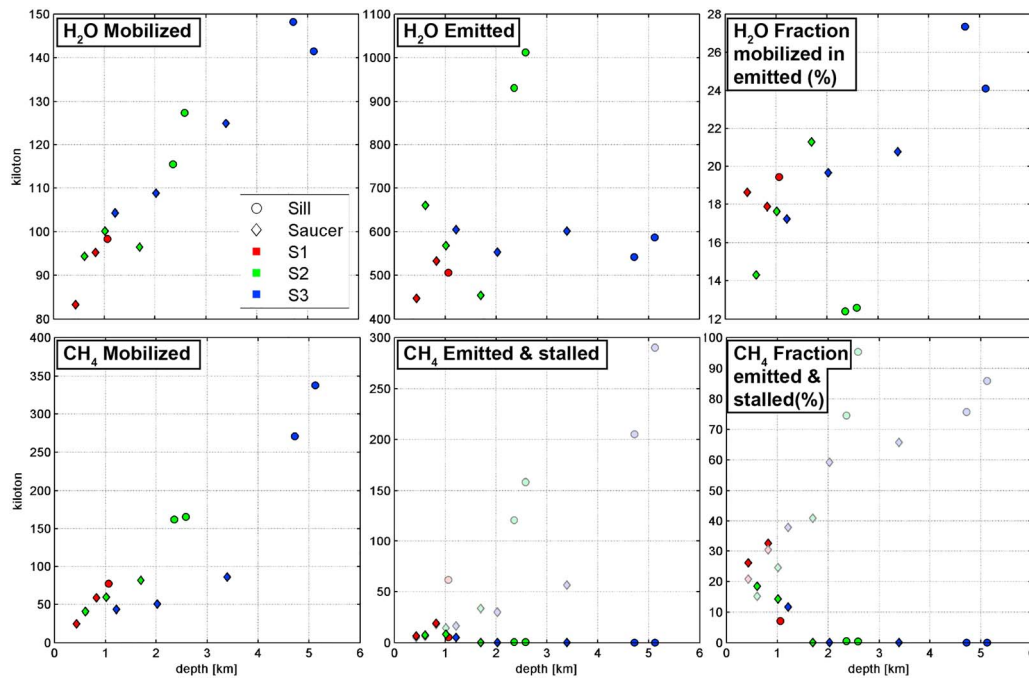


**Figure 7.** Quantification of the total water and methane mobilized at depth, emitted at the surface, and stalled on the way to the surface (for methane only) after the end of the hydrothermal activity. Shaded symbols represent the amount and fraction of methane stalled on the way to the surface. Values are reported in Table 3.

content with depth, and we observe an almost-linear increase of mobilized methane with increasing sill depth (Figure 7). This is due to (1) the increasing temperatures with depth that bring host-rocks closer to the degassing window and (2) to the increasing thickness of the organic-rich formations from the shallowest part of the basin represented with by section S1 to the deepest part of the basin represented by section S3. Methane emitted at the surface is a direct function of sill depth, showing increasing methane fraction emitted for decreasing sill depths (Figure 7). Our results indicate that, in the Karoo Basin conditions, degassing does not occur during the syn-hydrothermal phase for saucer-shaped sill beyond 1.7-km depth and for flat-lying sills beyond ~3-km depth (Figure 7 and Table 3).

In terms of quantity, flat-lying sills mobilize greater amounts of thermogenic methane than saucer-shaped sills in each basin section (Figure 7). This is due to the fact that their host-rocks are organic rich (2.8- to 4.5-wt.% TOC, Figure 2C), while the saucer-shaped sills emplace in organic-poor host-rock (0.5- to 1-wt.% TOC, Figure 2C). Additionally, we observe that saucer-shaped sills shallower than 1.7 km emit up to 30% of the mobilized methane from the basin. Finally, we report here the amount of methane stalled on the way to the surface at the end of the hydrothermal activity (Figure 7 and Table 3). Here we consider that only the methane above the sill horizon, because methane bearing fluids below the impermeable sill will be trapped. This quantity shows the same trend as the amount of methane mobilized at depth, that is, an increasing amount with increasing depth of the sills (regardless of the sill geometry, Figure 7 and Table 3). Deeper flat-lying sills produce highly concentrated methane plumes that rise but eventually stall on the way to the surface at the end of the hydrothermal fluid flow before any significant surface degassing occurs.

### 5.5. Basin Degassing Upscaling Quantification

The standard procedure to provide basin-scale estimate of thermogenic degassing is to upscale the amount obtained in simulations by relating the area of the sill considered with the global area of the sills inferred for the basin of interest (e.g., Aarnes et al., 2010; Iyer et al., 2013). Previous studies have conducted upscaling calculations on the basis of single simulation of saucer-shaped sills emplaced in a nonstratified environment. The variability of our results for different sill geometries and emplacement conditions shows that previous approaches are an oversimplification and cannot well represent a stratified basin of variable thickness. Our new calculations are tailored to represent the entire Karoo basin, taking into account variable host-

**Table 4**

Estimates of sill area in the overall Karoo Basin stratigraphy based on an average sill to host-rock sedimentary rock density of 19% for the Beaufort Group (Gp.) and 26% for the Eccca Group

Karoo Basin	Sectors	Area (km <sup>2</sup> )	Basement depth (km)	Volume of sedimentary rocks (km <sup>3</sup> )		
				Eccca Group	Beaufort Group	Total <sup>a</sup>
Sedimentary rocks	S1	309,928	1.2	88,949	215,710	371,913
	S2	137,752	2.9	92,983	225,225	399,482
	S3	55,036	5.7	74,299	179,696	313,708
	Total	502,716		256,231	620,904	1,085,103
		Number of sill levels		Volume of sills (km <sup>3</sup> )		
Sills		Eccca Group	Beaufort Group	Eccca Group	Beaufort Group	Total
	S1	1	2	23,127	40,985	64,112
	S2	2	3	24,175	42,793	66,968
	S3	2	3	19,318	34,194	53,512
			Total		66,620	117,972
				Area of sills (km <sup>2</sup> )		
Sills				Eccca Group	Beaufort Group	Total
			S1	231,270	409,850	641,120
			S2	241,750	427,930	669,680
			S3	193,180	341,940	535,120
			Total	666,200	1,179,720	1,845,900

Note. Borehole data used for this estimate can be found in Svensen et al. (2018). See supporting information S1–S3 for detailed statistical assementment.

<sup>a</sup>The total sedimentary rock volume includes all groups reported here (Beaufort and Eccca), as well as the Stormberg and Dwyka Groups.

rock properties at different sill emplacement depths and locations in the Karoo Basin. This section details a novel method to upscale our quantitative results without eluding the complexity of a basin stratification.

We have calculated the area of sills present in the different regions of the Karoo Basin for which our setups S1–S3 are representative (Table 4). To do this, we have estimated the Karoo Basin volume corresponding to each setup and each stratigraphic group containing sills (i.e., Beaufort Gp. and the Eccca Gp., Table 4). Based on borehole data published by Svensen et al. (2018), we have estimated that the volume fraction of sills correspond to 19% of the Beaufort Gp. and 26% of the Eccca Gp. (see supporting information S1 and Table S3.2 and Table 4). These percentages corresponds to a total surface area of sill of ~1,845,900 km<sup>2</sup>. Note that this area is nearly 5 times greater than a previous estimate of 370,000-km<sup>2</sup> sill intrusion area published for the Karoo Basin (Svensen et al., 2017). For comparison, this value would imply a sill proportion of only 3.4%. Area of sills corresponding to each of our three setups are detailed in Table 4. These values were used in our upscale calculations to obtain basin-scale estimates of thermogenic methane mobilized at depth and degassed at the basin top (Table 5).

Our result of ~30.9·10<sup>3</sup> Gt thermogenic methane mobilized at depth (Table 5) increases the maximum thermogenic gas mobilization potential of the Karoo Basin by a factor of 2. This increase is simply due to the larger surface area of the sills, which is 5 times greater than previously considered (Svensen et al., 2017). Remarkably, we find that despite the 5-times-greater surface area of sills, the amount of thermogenic gas emitted at the basin top during the hydrothermal activity, that is, ~1.6·10<sup>3</sup> Gt (Table 5), corresponds to the lowest bounds of previous estimates for the Karoo (Aarnes et al., 2010; Iyer et al., 2013). Note that we would have obtained an even smaller value if we had considered a sill volume fraction of only 3.4% (i.e., value corresponding to 370,000 km<sup>2</sup>; Svensen et al., 2017).

Given the obtained overall budget of mobilized versus emitted thermogenic gas, we estimate that only 5% of the mobilized methane is emitted to the surface during the active hydrothermal fluid flow phase (Table 5). The most dramatic reduction in surface emission comes from the fact that flat-lying sills beyond 1-km depth and saucer-shaped sills beyond 1.7-km depth do not enable hydrothermal plumes to rise to the surface before the thermal energy has vanished. However, methane-bearing fluids have a compositional buoyancy, which may lead to a faster syn-hydrothermal ascent of methane plumes and a continuing post-hydrothermal upflow of methane-carrying fluids. We have therefore quantified the amount of the methane stalled above the sill at the end of the hydrothermal fluid flow as a potential source for cold methane seeps. The amount of methane trapped below the impermeable sills are quantified as permanently stored in the basin (Table 5

**Table 5**  
New Basin-Scale Estimates of Thermogenic Gas Mobilization and Emission for the Karoo Basin, South Africa

Methane	Mobilization (Gt)			Emission (Gt)			Stalled (Gt)			Stored (Gt)		
	S1	S2	S3	S1	S2	S3	S1	S2	S3	S1	S2	S3
<b>B3</b>	—	1,002	850	—	184	99	—	152	322	—	666	429
<b>B2</b>	878	1,452	987	229	207	0	183	356	584	466	888	403
<b>B1</b>	2,063	2,003	1,682	672	0	0	628	819	1,105	763	1,184	577
<b>E2</b>	—	3,371	4,506	—	17	0	—	2,514	3,414	—	840	1,092
<b>E1</b>	3,071	3,446	5,615	220	16	0	2,460	3,291	4,827	391	138	788
<b>Subtotal</b>	6,012	11,274	13,640	1,122	425	99	3,271	7,133	10,251	1,620	3,716	3,289
<b>%</b>	—	—	—	3.5	1.4	0.3	10.6	23.1	33.2	5.2	12.0	10.6
<b>Total</b>	30,926			1,646			20,655			8,625		
<b>%</b>				5			67			28		

Note. These calculations are based on a total sill surface area of 1,845,900 km<sup>2</sup>, which corresponds to a sill volume fraction compared to the volume of sediments of 19% for the Beaufort Group and 26% for the Ecca Group. This average value is calculated on the basis of reported cumulative sill thicknesses observed in boreholes spread across the Karoo Basin (Svensen et al., 2018).

and Figure 8). The upscaled results show that the methane stalled on the way to the surface is an even greater source of methane degassing potential than the methane emitted during the active hydrothermal phase (Table 5 and Figures 7 and 9). A post-hydrothermal cold seep of the stalled methane would account for as

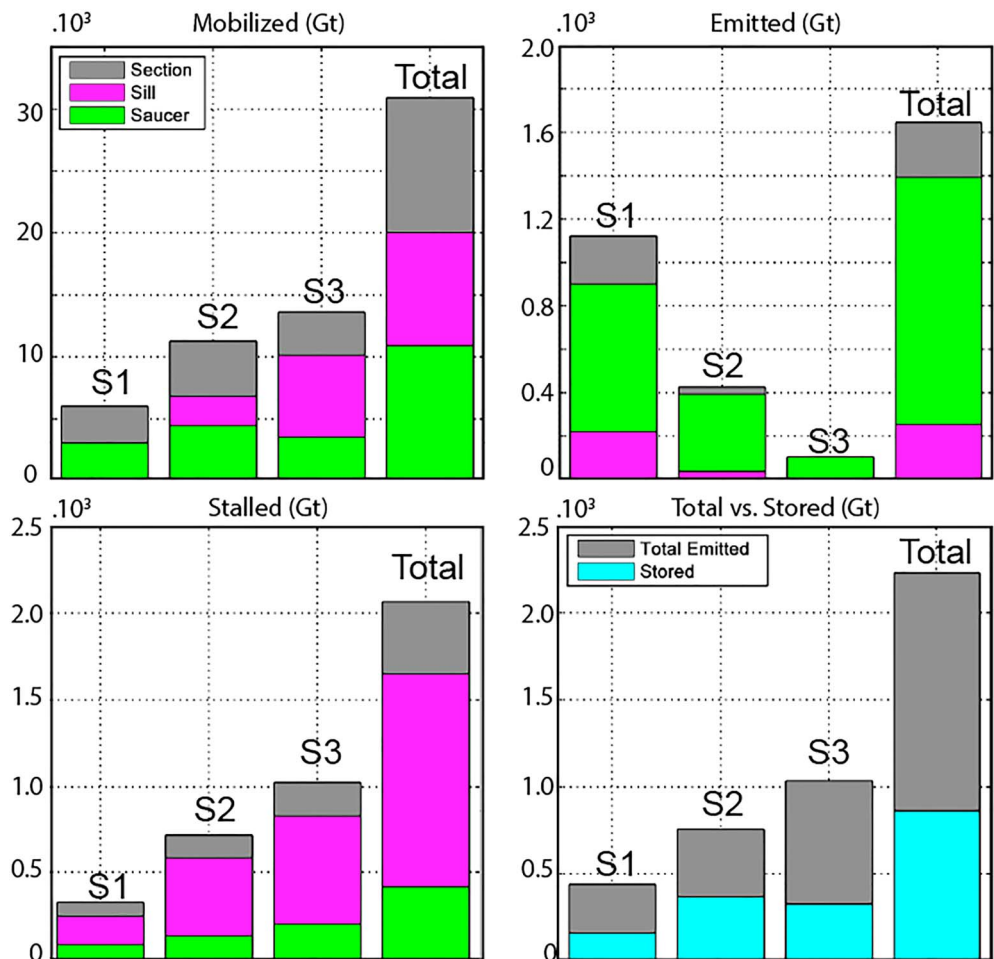


**Figure 8.** Summary of the upscaled quantities (mobilized, emitted, stalled, and stored) per section, using the described new upscaling method. Values are reported in Table 5.

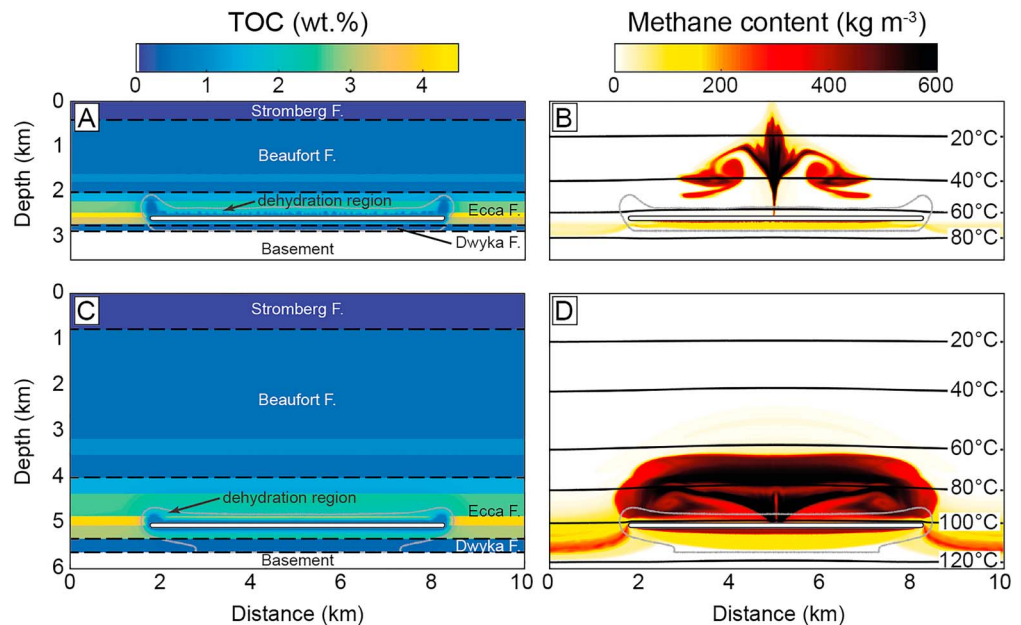


**Figure 9.** Examples of methane plumes stalling on the way to the surface at the end of the hydrothermal fluid flow (S2-E1 [A, B] and S3-E1 [C, D]). Left column (A, C) shows the remaining organic material present in the host rock, while the right column shows the methane concentration in the fluids. The significantly greater amount of methane in the deeper example S3-E1 (C, D), compared to the shallowest example S2-E1 (A, B), is explained by the greater thickness of the organic-rich lithologies for the deeper case (C). Black isotherms in all panels show only a slight deflection from the geothermal gradient, hence indicating that the transient heat anomalies of the sills and hydrothermal activity have vanished. TOC = total organic carbon.

much as  $\sim 20.7 \cdot 10^3$  Gt of methane emitted at the basin surface, that is, 67% of the methane mobilized at depth (e.g., S2-E1 and S3-E1, Figure 9). Considering the total surface emissions as the sum of the syn-hydrothermal (emitted) and post-hydrothermal (stalled) degassing, the Karoo Basin emissions amount to 72% of the mobilized methane, that is,  $\sim 22.3 \cdot 10^3$  Gt. These two degassing phases have distinct origins: 84% of the syn-hydrothermal surface emissions are attributed to the saucer-shaped sills and their hydrothermal vents, while 81% of the post-hydrothermal surface degassing is attributed to the deep flat-lying sills (Figure 7). In terms of quantity, post-hydrothermal potential surface emissions related to flat-lying sill are 12.5 times greater (i.e.,  $\sim 20.7 \cdot 10^3$  Gt, Figure 8) than those emitted by the saucer-shaped sills during the hydrothermal phase ( $\sim 1.6 \cdot 10^3$  Gt, Figure 8).

## 6. Discussion

### 6.1. Karoo Basin Degassing Model

Our result suggests that two distinct degassing pulses operate during the magma invasion of the Karoo Basin. These are associated with the two main types of lithologies that condition the sill geometry employed at different stratigraphic levels. The first degassing pulse is related to the HVCs rooting to the contact aureole of shallow saucer-shaped sills (<1.5 km) and is characterized by an early degassing with surface fluxes up to nearly 3 Gt/year within the first 100 years of emplacement (upscaled value from S1-B2, Table 3). Methane is primarily emitted by hot hydrothermal fluids (ranging between  $\sim 50$  and  $400$  °C, Table 3), and degassing lasts for 5,000 to 60,000 years (depending on the sill depth) at degassing rates above 100 Mt/year (S1-B1, S1-B2, S2-B2, S2-B3, and S3-B3). The second degassing pulse is a delayed surface methane flux carried by less hot water originating from flat-lying sills employed in the organic-rich strata of the Karoo Basin. The shallowest flat sills employed in the thinnest section of the basin (S1, 1-km depth, S1-E1) are the only ones that yield significant degassing during the syn-hydrothermal phase. For this particular example, the methane is carried by relatively warm fluids (48 °C) and degasses at a rate of up to 14,250 Mt/year. Degassing rates above 100 Mt/year last for a period of nearly 55,000 years. Deeper flat-lying sills only emit an insignificant fraction



**Table 6**  
*Fraction of Methane Emitted, Stalled, and Stored Compared to Methane Mobilized Per Section and Basin Wide*

Compared to methane mobilized		Emitted (%)			Stalled (%)			Stored (%)		
		S1	S2	S3	S1	S2	S3	S1	S2	S3
Per section	B3	—	1.6	0.7	—	1.3	2.4	—	5.9	3.1
	B2	3.8	1.8	0.0	3.0	3.2	4.3	7.8	7.9	3.0
	B1	11.2	0.0	0.0	10.5	7.3	8.1	12.7	10.5	4.2
	E2	—	0.2	0.0	—	22.3	25.0	—	7.4	8.0
	E1	3.7	0.1	0.0	41.0	29.2	35.4	6.5	1.2	5.8
	Subtotal	18.7	3.8	0.7	54.6	63.2	75.2	27.0	32.9	24.1
Basin wide	Subtotal	3.6	1.4	0.3	10.6	23.1	33.2	5.0	11.5	10.6
	Total	5			67			28		

*Note.* Gray highlights emphasize the absence of surface emission for the corresponding setups.

of methane, if at all, during the syn-hydrothermal phase (Table 5). These emissions are characterized by colder fluids (up to only 35 °C), which are often methane-free warm subsurface fluids that have not been near the sill at any time. Instead, they have been pushed upward by the deeper hydrothermal processes. Degassing rates reach a maximum 500 Mt/year (upscaled value from S2-E2), and rates above 100 Mt/year last for about 70,000 to 80,000 years (S2-E1 and S2-E2, Figure 6). These low emission rates, however, represent the mere onset of degassing from large methane plumes that rose from the flat sills and stalled before reaching the surface because thermal buoyancy vanished (Figure 9).

As mentioned above, compositional buoyancy could allow these methane-bearing fluids to accelerate and enable a complete surface emission through cold seeps during the syn-hydrothermal and post-hydrothermal phases. This would allow to emit the gas originating from the deeper sills. However, a second process is also likely to maintain high-surface degassing fluxes over the entire basin. The transient heat sources associated with the multiple sill intrusions emplaced all over the Karoo Basin overlap in time and sometimes in space (e.g., Golden Valley Sill Complex, Galerne et al., 2008; Galerne et al., 2010; Galerne et al., 2011; Galerne & Neumann, 2018) for a period of half a million years (Svensen et al., 2012). This implies, first, that stalled methane-bearing fluids could be remobilized by heat pulses coming from subsequent intrusions and, second, that the high-permeability networks formed by the various sills may interact to channel the thermogenic methane to the surface. This case would most likely have occurred at the Golden Valley Sill Complex (e.g., Galerne et al., 2008) where two levels of saucer-shaped sills are emplaced stacked on top of each other (Galerne et al., 2011). In this particular example, saucers come into contact without displaying chilled contacts (Galerne et al., 2010). This suggests a short time elapse between the emplacements of the two levels of saucer-shaped sills. Crucially, the large amounts of stalled methane plumes in some of our calculations highlight the importance of the time sequence of the magma invasion, which may control the amount and efficiency of thermogenic gas. Various end-member scenarios would translate into variable amounts mobilized and degassing rates. A scenario where shallow saucer-shaped sills emplace first would provide natural impermeable seals (fully crystallized sills) for the later gas migration. However, the high-permeability network around the cold shallow intrusions, left by earlier hydrothermal activity, may be reused and could assist in bypassing deeper methane-bearing fluids to the surface. On the contrary, a scenario where sills emplace progressively from the bottom up through the sedimentary column is a straightforward situation where a maximum volume of thermogenic gas can be released to the basin surface. Finally, new sills could emplace below or even within regions where methane-enriched fluids have migrated during the previous sill emplacement. Unfortunately, current dating technics do not allow the sequence of magma emplacement events during the Karoo LIP to be established.

Methane plumes revived by later transient heat sources would change the dynamics of syn-hydrothermal and post-hydrothermal degassing phase. Our calculations indicate that the various sectors of the Karoo Basin have each emitted 3.4/5th (shallowest sector S1), 1.3/5th (intermediate sector S2), and 0.3/5th (deepest sector S3) of the methane emitted during the syn-hydrothermal phase (Table 6). From these sections, those with the greatest amount of methane quantified as stalled in our study are those that would most likely degas most during subsequent sill intrusions, that is, S2: 23% and S3: 33% (see Figure 8 and Table 5 for

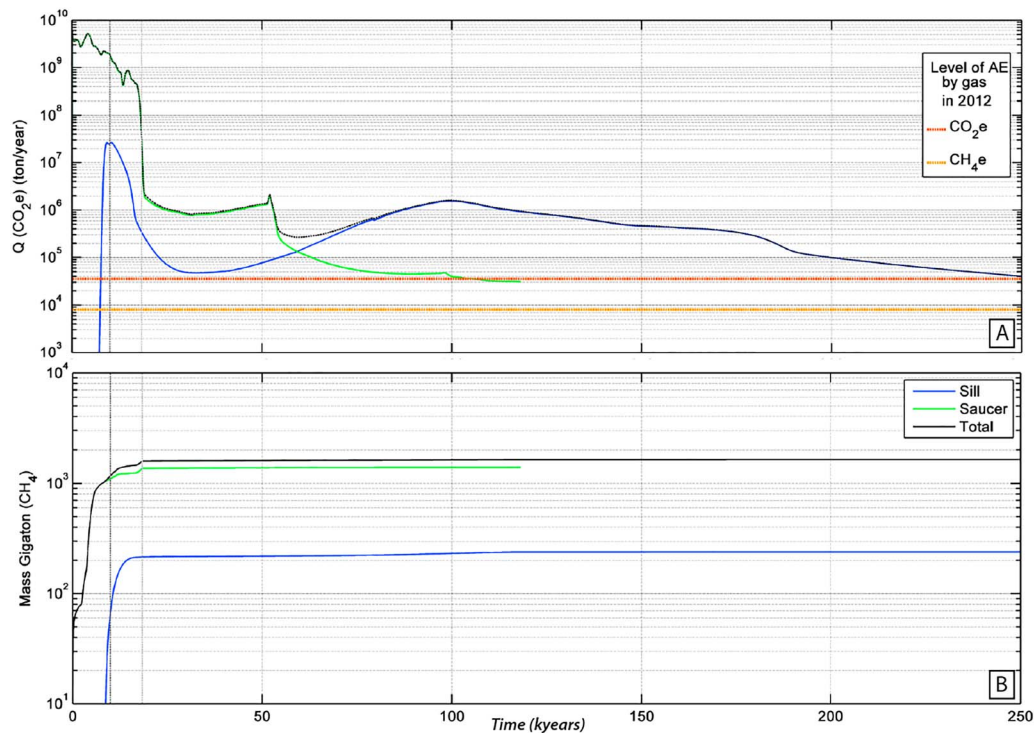


**Figure 10.** Hypothetical degassing scenario over 250,000 years, assuming a synchronous magma emplacement in the Karoo Basin. (A) Top curves are cumulative upscaled surface degassing fluxes for all flat-lying sills (blue), saucer-shaped sills (green), and combined (black). The two flat lines indicate the level of anthropogenic emission by gas for the year 2012, CO<sub>2</sub>e (orange) and CH<sub>4</sub>e (yellow). (B) Corresponding cumulative mass of methane emitted at the surface. Top values are expressed in CO<sub>2</sub>e, while bottom values are expressed for methane.

corresponding values). For these particular cases, multiple sill invasions enable to easily overcome the depth barrier for the saucer-shaped sills and flat-lying sills (1.5- and 3-km depths) allow large methane plumes to reach the surface.

In summary, the two distinct degassing pulses operating during the Karoo LIP event enable to degas the rim of the Karoo Basin (S1) as well as the overall shallowest ~1.5 km of the sedimentary host-rocks. This corresponds to a basin surface emission equivalent to 70 Mt of carbon (C) per kilometer cube of dolerite (calculated from emitted values Table 5), of which 61 Mt/km<sup>3</sup> are attributed to the shallow saucer-shaped sills. The late cold degassing attributed to the invasion of the deep organic-rich strata by flat-lying sills will most likely continue due to the buoyancy of the methane charged fluids. Together with multiple heat sources from subsequent intrusions, we estimate a total basin degassing equivalent to 1,363 Mt/km<sup>3</sup> of carbon (C), based on the stalled methane quantities (Table 5). From this value, flat-lying sills account for as much as 1,066 Mt/km<sup>3</sup> of carbon, representing by far the greatest threat for the paleo-environment of the Toarcian.

## 6.2. Implications for the Toarcian Environmental Crisis

To provide insights onto the Toarcian environmental crisis, we show a hypothetical scenario assuming that all intrusions have emplaced at the same time (Figure 10). The resulting cumulative degassing fluxes can be compared to present-day level of anthropogenic gas emissions expressed per gas in CO<sub>2</sub> equivalent (e) for the year 2012 (Ritchie & Roser, 2018). Our results indicate that the Karoo emission, at its peak, surpasses by nearly 5 orders of magnitude the amount of anthropogenic emissions of CH<sub>4</sub>e (Figure 10). These large degassing fluxes are maintained for a considerable period of 18,500 years, while anthropogenic emissions onset merely 168 years ago at the dawn of the industrial revolution in 1850 and only culminate at the reported level in 2012 (Ritchie & Roser, 2018). Given the quantified effect of anthropogenic emissions on present-day atmospheric temperature warming, ocean acidification, and world's climate in general, the consequences of the Karoo degassing can be considered as a prime, if not the main driver of the Toarcian environmental crisis.

Using a simple mass balance of carbon isotope reservoirs (Dickens et al., 1995), we calculate a  $\delta^{13}\text{C}$  value corresponding to a mass transfer equivalent to the thermogenic gas emitted during our simulations (syn-hydrothermal phase, Table 5). We use two distinct estimates for the mass of the various inorganic and organic carbon reservoirs involved in the mass balance (atmosphere, ocean, land biota, soil and humus, and dissolved marine). The results of  $-1.49\text{‰}$ , using Broecker and Peng (1993) values, and  $-1.83\text{‰}$ , using Siegenthaler (1993) values, are well within the range established by Cohen et al. (2007) based on geological records synchronous of the Karoo LIP. Even if we use only the amount emitted after 10,000 years in our hypothetical synchronous emplacement scenario (1,179 Gt, Figure 10B), we obtain values ranging from  $-1.07\text{‰}$  to  $-1.32\text{‰}$ . These values are still within the initial shift in the carbon record reported for the Toarcian event, that is, between  $-1.5$  and  $-3$  (Cohen et al., 2007).

We would like to emphasize here that scenarios accounting for the multiple sill invasion of the Karoo could emit a total of  $\sim 22.3 \cdot 10^3$  Gt of methane at the basin surface (13.5 times more than the amount quantified as emitted in Table 5). Although not tested here, these emplacement scenarios will provide valuable insights into possible surface degassing fluxes. Regardless of the actual sequence and hierarchy of magma emplacement in the Karoo LIP, we conclude that this volcanic event is well capable of accounting for a shift in  $\delta^{13}\text{C}$  at time scales of less than 10,000 years.

## 7. Summary and Conclusions

We have constructed a 2-D numerical model to simulate the complex hydraulic and mechanical interplay between contact metamorphism processes (dehydration and cracking) and hydrothermal fluid flow around cooling sill intrusions in a stratified, organic-rich, sedimentary basins. We have applied our numerical model to the well-documented Karoo Basin where we could assess a realistic proportion of sill to sediment for the main stratigraphic groups containing sills. The results of our calculations indicate the following:

- Only the shallow 1.5 km of the basin enable surface degassing before the heat originating from the cooling sills vanishes and the hydrothermal fluid flow stops. This degassing event is principally driven by the HVC related to the shallow saucer-shaped sills and amount to  $\sim 1.6 \cdot 10^3$  Gt of thermogenic methane.
- We have quantified that  $\sim 20.7 \cdot 10^3$  Gt of thermogenic methane from the deeper region of the basin remain trapped on the way to the surface. We argue here that the bulk of these stalled methane plumes could have been emitted at the basin surface in reality. Possible mechanisms are the natural buoyancy of the methane charged fluids (which we did not include in our calculations) and subsequent transient heat sources arising from later sill intrusions. This second mechanism would allow the remobilization of methane-bearing fluids to bring them further upward toward the surface. Degassing of the methane plumes triggered by the deepest sills emplaced in the thick organic-rich sections of the Ecca Formation (Figure 9) are by far the greater threat to the paleo-environment of the Toarcian.

Surface degassing fluxes arising from the high-permeability channels linking the surface to the edge of the shallow sill intrusions indicate

- a rapid onset of degassing within the first 100 years of the saucer-shaped sill cooling
- high degassing rates that last for 5,000 to 60,000 years at level above 100 Mt/year

However, we conclude here that the largest amount of degassing will be carried out by cold fluids. Such cold emissions will occur for a large portion during the initial degassing as a precursor of the hot hydrothermal fluids and in a later stage through compositional buoyancy or revived thermal buoyancy due to subsequent sill intrusion.

Finally, we have calculated that the amount of methane emitted, during what we termed syn-hydrothermal phase, is sufficient to shift  $\delta^{13}\text{C}$  values by  $-1.49\text{‰}$  to  $-1.83\text{‰}$ . These are in range of values reported for the Toarcian event. We have also shown through a hypothetical synchronous emplacement scenario that this level of emission can occur shortly after the intrusions start to cool and crystallize on a time scale of 10,000 years. Overall, we propose that the Karoo has emitted as much  $\sim 22.3 \cdot 10^3$  Gt of thermogenic methane to the ocean atmosphere system of the Toarcian. This estimate nearly doubles former most pessimistic calculations making the Karoo LIP the greatest source of thermogenic methane emitted during a LIP event. We therefore conclude that the Karoo LIP plumbing system was the main driver for the Toarcian environmental crisis and that the potent nature of similar geological events on paleo-environments may have been largely underestimated.

### Acknowledgments

The authors would like to thank Prof. Christian Berndt for supporting Dr. Christophe Galerne in his research at the Department of Marine Geodynamics of the GEOMAR Helmholtz Centre for Ocean Research Kiel. We also thank Prof. Lars Rüpke and the Department of Ocean Resources for supporting the initial work of this study. Finally, the authors would like to thank Steffi Burchardt and two anonymous reviewers for their constructive reviews. Complementary data related to the publication can be found at PANGAEA (Data Publisher for Earth and Environment Science: <https://doi.pangaea.de/10.1594/PANGAEA.900982>).

### References

- Aarnes, I., Planke, S., Trulsvik, M., & Svensen, H. (2015). Contact metamorphism and thermogenic gas generation in the Vøring and Møre basins, offshore Norway, during the Paleocene-Eocene thermal maximum. *Journal of the Geological Society*, *172*(5), 588–598. <https://doi.org/10.1144/jgs2014-098>
- Aarnes, I., Svensen, H., Connolly, J. A. D., & Podladchikov, Y. Y. (2010). How contact metamorphism can trigger global climate changes: Modeling gas generation around igneous sills in sedimentary basins. *Geochimica et Cosmochimica Acta*, *74*(24), 7179–7195. <https://doi.org/10.1016/j.gca.2010.09.011>
- Aarnes, I., Svensen, H., Polteau, S., & Planke, S. (2011). Contact metamorphism devolatilization of shales in the Karoo Basin, South Africa, and the effects of multiple sill intrusions. *Chemical Geology*, *281*(3–4), 181–194. <https://doi.org/10.1016/j.chemgeo.2010.12.007>
- Abdelmalak, M. M., Mourgues, R., Galland, O., & Bureau, D. (2012). Fracture mode analysis and related surface deformation during dyke intrusion: Results from 2D experimental modelling. *Earth and Planetary Science Letters*, *359–360*, 93–105. <https://doi.org/10.1016/j.epsl.2012.10.008>
- Andersen, C., Rüpke, L. H., Hasenclever, J., Grevemeyer, I., & Petersen, S. (2015). Fault geometry and permeability contrast control vent temperatures at the Logatchev 1 hydrothermal field, Mid-Atlantic Ridge. *Geology*, *43*(1), 51–54. <https://doi.org/10.1130/g36113.1>
- Athy, L. F. (1930). Density, porosity and compaction of sedimentary rocks. *American Association of Petroleum Geologists Bulletin*, *14*, 1–24.
- Baiyegunhi, C., Oloniniyi, T. L., & Gwavava, O. (2014). The correlation of dry density and porosity of some rocks from the Karoo Supergroup: A case study of selected rock types between Grahamstown and Queenstown in the Eastern Cape Province, South Africa. *IOSR Journal of Engineering*, *4*(12), 30–40.
- Beardsmore, G. R., & Cull, J. P. (2001). *Crustal heat flow*. Cambridge, U.K.: Cambridge University Press. <https://doi.org/10.1017/CBO9780511606021>
- Berndt, C., Hensen, C., Mortera-Gutierrez, C., Sarkar, S., Geilbert, S., Schmidt, M., et al. (2016). Rifting under steam—How rift magmatism triggers methane venting from sedimentary basins. *Geology*, *44*(9), 767–770. <https://doi.org/10.1130/G38049.1>
- Blackburn, T., Oslen, P. E., Bowring, S. A., McLean, N. M., Kent, D. V., Puffer, J., et al. (2013). Zircon U-Pb geochronology links the end-triassic extinction with the central Atlantic magmatic province. *Science*, *340*(6135), 941–945. <https://doi.org/10.1126/science.1234204>
- Branch, T., Ritter, O., Weckmann, U., Sachsenhofer, R. F., & Schilling, F. (2007). The Whitehill Formation—A high conductivity marker horizon in the Karoo Basin. *South African Earth Sciences*, *18*(3), 227–243.
- Broecker, W. S., & Peng, T.-H. (1993). What caused the glacial to interglacial CO<sub>2</sub> change? In M. Heinmann (Ed.), *The Global Carbon Cycle, NATO ASI Ser. I*, (Vol. 15, pp. 95–115).
- Burgess, S. D., Bowring, S. A., Fleming, T. H., & Elliot, D. H. (2015). High-precision geochronology links the Ferrar large igneous province with early-Jurassic ocean anoxia and biotic crisis. *Earth and Planetary Science Letters*, *415*, 90–99. <https://doi.org/10.1016/j.epsl.2015.01.037>
- Campbell, S. A., Lenhardt, N., Dippenaar, M. A., & Götz, A. (2016). Geothermal energy from the Main Karoo Basin (South Africa): An outcrop analogue study of Permian sandstone reservoir formations. *Energy Procedia*, *97*, 186–193. <https://doi.org/10.1016/j.egypro.2016.10.050>
- Campbell, S. A., Mielke, P., & Götz, A. (2016). Geothermal energy from the Main Karoo Basin? New insights from borehole KKW-1 (Eastern Cape South Africa). *Geothermal Energy*, *4*(9), 1–19.
- Cartwright, J., & Hansen, D. M. (2006). Magma transport through the crust via interconnected sill complexes. *Geology*, *34*(11), 929–932. <https://doi.org/10.1130/G22758A.1>
- Catuneanu, O., Hancox, P. J., & Rubidge, B. S. (1998). Reciprocal flexural behaviour and contrasting stratigraphies: A new basin development model for the Karoo retroarc foreland system, South Africa. *Basin Research*, *10*(4), 417–439. <https://doi.org/10.1046/j.1365-2117.1998.00078.x>
- Chevallier, L., & Woodford, A. (1999). Morpho-tectonics and mechanism of emplacement of the dolerite rings and sills of the western Karoo, South Africa. *South African Journal of Geology*, *102*(1), 43–54.
- Cohen, A. S., Coe, A. L., & Kamp, D. B. (2007). The Late Paleocene Early Eocene and Toarcian (Early Jurassic) carbon isotope excursions: A comparison of their time scales, associated environmental changes, causes and consequences. *Journal of the Geological Society*, *164*(6), 1093–1108. <https://doi.org/10.1144/0016-76492006-123>
- Connolly, J. A. D. (2009). The geodynamic equation of state: What and how. *Geochemistry, Geophysics, Geosystem*, *10*, 10, Q10014. <https://doi.org/10.1029/2009GC002540>
- Costa, A. (2006). Permeability-porosity relationship: A re-examination of the Kozeny-Carman equation based on a fractal pore-space geometry assumption. *Geophysical Research Letters*, *33*, L02318. <https://doi.org/10.1029/2005GL025134>
- Čermák, V., & Rybach, L. (1982). Thermal properties—Thermal conductivity and specific heat of minerals and rocks. In G. Angenheister (Ed.), *Physical properties of rocks*, (Vol. 1, Subvolume A, pp. 305–343).
- Dhansay, T., Musekiwa, C., Ntholi, T., Chevallier, L., Cole, D., & de Wit, M. J. (2017). South Africa's geothermal energy hotspots inferred from subsurface temperature and geology. *South African Journal of Science*, *113*(11/12), 7. <https://doi.org/10.17159/sajs.2017/20170092>
- Dickens, G. R., O'Neil, J. R., Rea, D. K., & Owen, R. M. (1995). Dissociation of oceanic methane hydrate as a cause of the carbon isotope excursion at the end of the Paleocene. *Paleoceanography*, *10*(6), 965–971. <https://doi.org/10.1029/95PA02087>
- Dow, W. G. (1977). Kerogen studies and geological interpretations. *Journal of Geochemical Exploration*, *7*, 79–99. [https://doi.org/10.1016/0375-6742\(77\)90078-4](https://doi.org/10.1016/0375-6742(77)90078-4)
- Du Toit, A. L. (1920). The Karoo dolerites—A study in hypabyssal intrusion. *Transaction of the Geological Society of Africa*, *23*, 1–42.
- EIA (2015). Technically recoverable shale oil and shale gas resources: South Africa. U.S. Energy Information Administration.
- Faure, K., & Cole, D. (1999). Geochemical evidence for lacustrine microbial blooms in the vast Permian Main Karoo, Parana, Falkland Islands and Huab basins of southwestern Gondwana. *Paleogeography, Paleoclimatology, Paleoecology*, *152*(3–4), 189–213. [https://doi.org/10.1016/S0031-0182\(99\)00062-0](https://doi.org/10.1016/S0031-0182(99)00062-0)
- Galerie, C. Y., Galland, O., Neumann, E.-R., & Planke, S. (2011). 3D relationships between sills and their feeders: Evidence from geological data, geochemistry and experimental modelling. *Journal of Volcanology and Geothermal Research*, *202*(3–4), 189–199. <https://doi.org/10.1016/j.jvolgeores.2011.02.006>
- Galerie, C. Y., & Neumann, E.-R. (2018). Geochemical fingerprinting and magmatic plumbing systems. In C. Breitkreuz, & S. Rocchi (Eds.), *Laccoliths, sills and dykes—Physical geology of shallow magmatic systems. Advances in volcanology* (pp. 119–130). [https://doi.org/10.1007/11157\\_2014\\_4](https://doi.org/10.1007/11157_2014_4)

- Galerne, C. Y., Neumann, E.-R., Aarnes, I., & Planke, S. (2010). Magmatic differentiation processes in saucer-shaped sills: Evidence from the Golden Valley Sill in the Karoo Basin, South Africa. *Geosphere*, 6(3), 163–188. <https://doi.org/10.1130/GES00500.1>
- Galerne, C. Y., Neumann, E.-R., & Planke, S. (2008). Emplacement mechanisms of sill complexes: Information from the geochemical architecture of the Golden Valley Sill Complex, South Africa. *Journal of Volcanology and Geothermal Research*, 177(2), 425–440. <https://doi.org/10.1016/j.jvolgeores.2008.06.004>
- Galland, O. (2012). Experimental modelling of ground deformation associated with shallow magma intrusions. *Earth and Planetary Science Letters*, 317, 145–156.
- Galland, O., Bertelsen, H., Haug Eider, C., Guldstrand, F., Haug, Ø. T., Leanza, H. A., et al. (2018). Storage and transport of magma in the layered crust-formation of sills and related flat-lying intrusions. In S. Burchardt (Ed.), *Volcanic and igneous plumbing systems* (pp. 112–138). <https://doi.org/10.1016/B978-0-12-809749-6.00005-4>
- Galland, O., Planke, S., Neumann, E. R., & Malthe-Sørenssen, A. (2009). Experimental modelling of shallow magma emplacement: Application to saucer-shaped intrusions. *Earth and Planetary Science Letters*, 277(3–4), 373–383. <https://doi.org/10.1016/j.epsl.2008.11.003>
- Galland, O., & Scheibert, J. (2013). Analytical model of surface uplift above axisymmetric flat-lying magma intrusions: Implications for sill emplacement and geodesy. *Journal of Volcanology and Geothermal Research*, 253, 114–130. <https://doi.org/10.1016/j.jvolgeores.2012.12.006>
- Ganino, C., & Arndt, N. T. (2009). Climate changes caused by degassing of sediments during the emplacement of large igneous provinces. *Geology*, 37(4), 323–326. <https://doi.org/10.1130/G25325A.1>
- Hansen, D. M., & Cartwright, J. (2006). The three-dimensional geometry and growth of forced folds above saucer-shaped igneous sills. *Journal of Structural Geology*, 28(8), 1520–1535. <https://doi.org/10.1016/j.jsg.2006.04.004>
- Hansen, D. M., & Cartwright, J. (2007). Reply to comment by K. Thomson on “The three-dimensional geometry and growth of forced folds above saucer-shaped sills” by D.M., Hansen and J. Cartwright. *Journal of Structural Geology*, 29(4), 741–744. <https://doi.org/10.1016/j.jsg.2006.10.008>
- Hansen, D. M., Cartwright, J., & Thomas, D. (2004). 3D seismic analysis of the geometry of igneous sills and sill junctions relationships. In R. J. Davies, J. Cartwright, S. A. Stewart, M. Lappin, & J. R. Underhill (Eds.), *3D seismic technology: Application to the exploration of sedimentary basins*, Geological Society, (pp. 199–208). London: Memoirs.
- Hanson, R. E., & Elliot, D. H. (1996). Rift-related Jurassic basaltic phreatomagmatic volcanism in the central Transantarctic Mountains: Precursory stage to flood-basalt effusion. *Bulletin of Volcanology*, 58(5), 327–347. <https://doi.org/10.1007/s004450050143>
- Hasenclever, J., Theissen-Krah, S., Rüpke, L. H., Phipps Morgan, J., Iyer, K., Petersen, S., & Devey, C. W. (2014). Hybrid shallow on-axis and deep off-axis hydrothermal circulation at fast-spreading ridges. *Nature*, 508(7497), 508–512. <https://doi.org/10.1038/nature13174>
- Haug, Ø. T., Galland, O., Souloumiac, P., Souche, A., Guldstrand, F., Scmiedel, T., & Maillot, B. (2018). Shear versus tensile failure mechanisms induced by sill intrusions—Implications for emplacement of conical and saucer-shaped intrusions. *Journal of Geophysical Research: Solid Earth*, 123, 3430–3449. <https://doi.org/10.1002/2017JB015196>
- Heydari, E., Arzani, N., & Hassanzadeh, J. (2008). Mantle plume: The invisible serial killer—Application to the Permian-Triassic boundary mass extinction. *Paleogeography, Paleoclimatology, Paleocology*, 264(1–2), 147–162. <https://doi.org/10.1016/j.palaeo.2008.04.013>
- Iyer, K., Rüpke, L., & Galerne, C. Y. (2013). Modeling fluid flow in sedimentary basins with sill intrusions: Implications for hydrothermal venting and climate change. *Geochemistry, Geophysics, Geosystems*, 14, 5244–5262. <https://doi.org/10.1002/2013GC005012>
- Iyer, K., Schmid, D. W., Planke, S., & Millett, J. (2017). Modelling hydrothermal venting in volcanic sedimentary basins: Impact on hydrocarbon maturation and paleoclimate. *Earth and Planetary Science Letters*, 467, 30–42. <https://doi.org/10.1016/j.epsl.2017.03.023>
- Iyer, K., Svensen, H., & Schmidt, D. W. (2018). SILLi 1.0: A 1-D numerical tool quantifying the thermal effects of sill intrusions. *Geoscientific Model Development*, 11(1), 43–60. <http://doi.org/10.5194/gmd-11-43-2018>
- Jamtveit, B., Svensen, H., Podladchikov, Y. Y., & Planke, S. (2004). Hydrothermal vent complexes associated with sill intrusions in sedimentary basins. In C. Breitreuz, & N. Petford (Eds.), *Physical geology of high-level magmatic systems*, Geological Society, (pp. 233–241). London: Special Publication.
- Johnson, M. R., Van Vuuren, C. J., Hegenberger, W. F., Key, R., & Shoko, U. (1996). Stratigraphy of the Karoo Supergroup in southern Africa: An overview. *Journal of African Earth Sciences*, 23(1), 3–15. [https://doi.org/10.1016/S0899-5362\(96\)00048-6](https://doi.org/10.1016/S0899-5362(96)00048-6)
- Johnson, M. R., Van Vuuren, C. J., Visser, J. N. J., Cole, D. I., de Wickens, H. V., Christie, A. D. M., et al. (2006). Sedimentary rocks of the Karoo Supergroup. In M. R. Johnson, C. R. Anhaeusser, & R. J. Thomas (Eds.), *The geology of South Africa*, (pp. 461–499). Pretoria: Geological Society of South Africa/Council for Geosciences.
- Jones, M., Jerram, D. A., Svensen, H., & Grove, C. (2016). The effects of large igneous provinces on the global carbon and sulphur cycles. *Paleogeography, Paleoclimatology, Paleocology*, 441.
- Jones, M. Q. W. (1993). *Heat flow in South Africa. Handbook of the Geological Survey no. 14*, (p. 174). Pretoria.
- Kjeldstad, A., Langtangen, H., Skogseid, J., & Bjørlykke, K. (2003). Simulation of sedimentary basins. In H. Langtangen, & A. Tveit (Eds.), *Advanced topics in computational partial differential equations: Numerical methods and Diffpack Programming*, (pp. 611–658). New York: Springer-Verlag. [https://doi.org/10.1007/978-3-642-18237-2\\_15](https://doi.org/10.1007/978-3-642-18237-2_15)
- Laske, G., Masters, G., Ma, Z., & Pasyanos, M. (2013). Update on CRUST1.0—A 1-degree global model of Earth's crust. *Geophysical Research Abstracts*, 15.
- Malthe-Sørenssen, A., Planke, S., Svensen, H., & Jamtveit, B. (2004). Formation of saucer-shaped sills. In C. Breitreuz, & N. Petford (Eds.), *Physical geology of high-level magmatic systems*, Geological Society, (pp. 215–227). London: Special Publication.
- Mathieu, L., van de Wyk Vries, B., Holohan, E. P., & Troll, V. R. (2008). Dykes, cups, saucers and sills: Analogue experiments on magma intrusion into brittle rocks. *Earth and Planetary Science Letters*, 271(1–4), 1–13. <https://doi.org/10.1016/j.epsl.2008.02.020>
- McKay, D. I. A., Tyrrell, T., Wilson, P. A., & Foster, G. L. (2014). Estimating the impact of the cryptic degassing of large igneous provinces: A mid-Miocene case-study. *Earth and Planetary Science Letters*, 403, 254–262. <https://doi.org/10.1016/j.epsl.2014.06.040>
- Merle, O., & Donnadieu, F. (2000). Indentation of volcanic edifices by the ascending magma. In B. Vendeville, Y. Mart, & J.-L. Vigneresse (Eds.), *Salt, shale and igneous diapirs in and around Europe*, (Vol. 174, pp. 43–53). Geological Society, London, Special Publications. <https://doi.org/10.1144/GSL.SP.1999.174.01.03>
- Nichols, G. T., Wyllie, P. J., & Stern, C. R. (1994). Subduction zone melting of pelagic sediments constrained by melting experiments. *Nature*, 371(6500), 785–788. <https://doi.org/10.1038/371785a0>
- Planke, S., Rasmussen, T., Rey, S.S., & Myklebust, R. (2005). Seismic characteristics and distribution of volcanic intrusions and hydrothermal vent complexes in the Voring and Møre basins. In A.G. Doré, & B.A. Vining (Eds.), *Petroleum geology: North-West Europe*

- and global perspectives—*Proceedings of the 6th Petroleum Geology Conference*, 833–844. © Petroleum Geology Conferences Ltd. Published by the Geological Society, London.
- Planke, S., & Symonds, P. A. (2000). Seismic volcanostratigraphy of large-volume basaltic extrusive complexes on rifted margins. *Journal of Geophysical Research*, 105, 19,335–19,351.
- Pollard, D. D., & Johnson, A. M. (1973). Mechanics of growth of some laccolithic intrusions in the Henry Mountains, Utah, II. *Tectonophysics*, 18(3–4), 311–354. [https://doi.org/10.1016/0040-1951\(73\)90051-6](https://doi.org/10.1016/0040-1951(73)90051-6)
- Retallack, G. J., & Jahren, A. H. (2008). Methane release from igneous intrusion of coal during late Permian extinction events. *The Journal of Geology*, 116(1), 1–20. <https://doi.org/10.1086/524120>
- Ritchie, H., & Roser, M. (2018). CO2 and other greenhouse gas emissions. Published online at OurWorldInData.org. Retrieved from: <https://ourworldindata.org/co2-and-other-greenhouse-gas-emissions>
- Rowell, D. M., & De Swardt, A. M. J. (1976). Diagenesis in Cape and Karoo sediments, South Africa, and its bearing on their hydrocarbon potential. *Transactions, Geological Society of South Africa*, 79(1), 81–154.
- Schmiedel, T., Kjøberg, S., Planke, S., Magee, C., Galland, O., Schofield, N., et al. (2017). Mechanisms of overburden deformation associated with the emplacement of the Tulipan sill, mid-Norwegian margin. *Interpretation*, 5(3), SK23–SK38. <https://doi.org/10.1190/INT-2016-0155.1>
- Siegenthaler, U. (1993). Modeling the present-day ocean carbon cycle. In M. Heinmann (Ed.), *The Global Carbon Cycle, NATO ASI Ser. I*, (Vol. 15, pp. 367–395).
- Spacapan, J. B., Galland, O., Leanza, H. A., & Planke, S. (2016). Igneous sill and finger emplacement mechanism in shale-dominated formations: A field study at Cuesta del Chihuido, Neuquén Basin, Argentina. *Journal of the Geological Society*, 174(3), 422–433. <https://doi.org/10.1144/jgs2016-056>
- Stockley, G. M. (1947). *Report on the geology of Basutoland*. Maseru: Published by the authority of the Basutoland Government.
- Svensen, H., Corfu, F., Polteau, S., Hammer, O., & Planke, S. (2012). Rapid magma emplacement in the Karoo Large Igneous Province. *Earth and Planetary Science Letters*, 325, 1–9.
- Svensen, H., Jamtveit, B., Planke, S., & Chevallier, L. (2006). Structure and evolution of hydrothermal vent complexes in the Karoo Basin, South Africa. *Journal of the Geological Society*, 163(4), 671–682. <https://doi.org/10.1144/1144-764905-037>
- Svensen, H., Planke, S., Chevallier, L., Malthes-Sorensen, A., Corfu, F., & Jamtveit, B. (2007). Hydrothermal venting of greenhouse gases triggering Early Jurassic global warming. *Earth and Planetary Science Letters*, 256(3–4), 554–566. <https://doi.org/10.1016/j.epsl.2007.02.013>
- Svensen, H., Planke, S., Malthes-Sorensen, A., Jamtveit, B., Myklebust, R., Eidem, T. R., & Rey, S. S. (2004). Release of methane from a volcanic basin as a mechanism for initial Eocene global warming. *Nature*, 429(6991), 542–545. <https://doi.org/10.1038/nature02566>
- Svensen, H., Planke, S., Polozov, A. G., Schmidbauer, N., Corfu, F., Podladchikov, Y. Y., & Jamtveit, B. (2009). Siberian gas venting and the end-Permian environmental crisis. *Earth and Planetary Science Letters*, 227, 490–500.
- Svensen, H., Polteau, S., Cawthorn, G., & Planke, S. (2018). Sub-volcanic intrusions in the Karoo Basin, South Africa. In C. Breitreuz, & S. Rocchi (Eds.), *Laccoliths, sills and dykes—Physical geology of shallow magmatic systems, Advances in Volcanology* (pp. 349–362).
- Svensen, H., Torsvik, T. H., Callegaro, S., Augland, L., Heimdal, T. H., Jerram, D. A., et al. (2017). Gondwana Large Igneous Provinces: Plate reconstructions, volcanic basins and sill volumes. In S. Sensarma, & B. C. Storey (Eds.), *Large igneous provinces from Gondwana and adjacent regions*, (Vol. 463, pp. 17–40). Geological Society, London, Special Publications. <https://doi.org/10.1144/SP463.7>
- Sweeney, J., & Burnham, A. K. (1990). Evaluation of a simple model of vitrinite reflectance based on chemical kinetics. *American Association of Petroleum Geologists Bulletin*, 74(10), 1559–1570.
- Tankard, T., Welsink, H., Aukes, P., Newton, R., & Stettler, E. (2009). Tectonic evolution of the Cape and Karoo basins of South Africa. *Marine and Petroleum Geology*, 26(8), 1379–1412. <https://doi.org/10.1016/j.marpetgeo.2009.01.022>
- Thomson, K. (2005). Volcanic features of the North Rockall Trough: Application of visualisation techniques on 3D seismic reflection data. *Bulletin of Volcanology*, 67(2), 116–128. <https://doi.org/10.1007/s00445-004-0363-9>
- Thomson, K. (2007). Determining magma flow in sills, dykes and laccoliths and their implications for sill emplacement. Mechanisms. *Bulletin of Volcanology*, 70(2), 183–201. <https://doi.org/10.1007/s00445-007-0131-8>
- Thomson, K., & Hutton, D. H. W. (2004). Geometry and growth of sill complexes: Insights using 3D seismic from the North Rockall Trough. *Bulletin of Volcanology*, 66(4), 364–375. <https://doi.org/10.1007/s00445-003-0320-z>
- Vehling, F., Hasenclever, J., & Rüpke, L. (2018). Implementation strategies for accurate and efficient control volume-based two-phase hydrothermal flow solutions. *Transport in Porous Media*, 121(2), 233–261. <https://doi.org/10.1007/s11242-017-0957-2>
- Weis, P. (2015). The dynamic interplay between saline fluid flow and rock permeability in magmatic-hydrothermal systems. *Geofluids*, 15(1–2), 350–371. <https://doi.org/10.1111/gfl.12100>
- White, J. D. L., & McClintock, M. K. (2001). Immense vent complex marks flood-basalt eruption in a wet, failed rift: Coombs Hills, Antarctica. *Geology*, 29(10), 935–938. [https://doi.org/10.1130/0091-7613\(2001\)029<0935:IVCMFB>2.0.CO;2](https://doi.org/10.1130/0091-7613(2001)029<0935:IVCMFB>2.0.CO;2)
- Woodford, A. C., Botha, J. F., & Chevallier, L. (2001). Hydrogeology of the main Karoo Basin: Current knowledge and research needs. *Water Research Commission Pretoria*, Report, 860.

## References From the Supporting Information

- Bostick, N. H., & Pawlewicz, M. J. (1984). Paleotemperatures based on vitrinite reflectance of shales and limestones in igneous dike aureoles in the Upper Cretaceous Pierre Shale, Walsenburg, Colorado. In Hydrocarbon source rocks of the greater Rocky Mountain region. In J. G. Woodward, F. F. Meissner, & C. J. Clayton (Eds.), *Rocky Mountain Association of Geologists*, (pp. 387–392).